Monthly Notices of the ROYAL ASTRONOMICAL SOCIETY

MNRAS **541,** 29–45 (2025)
Advance Access publication 2025 June 17

https://doi.org/10.1093/mnras/staf993

Unveiling faint X-ray AGN populations in the NewAthena era: insights from cosmological simulations

Nuno Covas,[1,2]★ Israel Matute,[1,2] Stergios Amarantidis,[3] José Afonso,[1,2] Giorgio Lanzuisi,[4] Andrea Comastri,[4] Stefano Marchesi,[4,5,6] Ciro Pappalardo,[1,2] Rodrigo Carvajal[1,2] and Polychronis Papaderos[7]

[1]*Instituto de Astrofísica e Ciências do Espaço, Universidade de Lisboa- OAL, Tapada da Ajuda, PT1349-018 Lisboa, Portugal*
[2]*Departamento de Física, Faculdade de Ciências da Universidade de Lisboa, Edifício C8, Campo Grande, PT1749-016 Lisboa, Portugal*
[3]*Institut de Radioastronomie Millimétrique (IRAM), Avenida Divina Pastora 7, Local 20, E-18012, Granada, Spain*
[4]*INAF, Osservatorio di Astrofisica e Scienza dello Spazio (OAS) di Bologna, via P. Gobetti 93/3, I-40129 Bologna, Italy*
[5]*Dipartimento di Fisica e Astronomia (DIFA), Università di Bologna, via Gobetti 93/2, I-40129 Bologna, Italy*
[6]*Department of Physics and Astronomy, Clemson University, Kinard Lab of Physics, Clemson, SC 29634, USA*
[7]*Instituto de Astrofísica e Ciências do Espaço, Universidade do Porto–CAUP, Rua das Estrelas, PT4150-762 Porto, Portugal*

Accepted 2025 June 13. Received 2025 June 10; in original form 2025 April 15

ABSTRACT

Recent observations expanded our understanding of galaxy formation and evolution, yet key challenges persist in the X-ray regime, crucial for studying active galactic nuclei (AGNs). These limitations drive the development of next-generation observatories such as ESA's NewAthena. Now in phase B (preliminary design), the mission requires extensive testing to ensure compliance with its scientific goals, particularly given the uncertainties surrounding high-redshift AGN. This work leverages the ILLUSTRISTNG cosmological simulation to build an X-ray AGN mock catalogue and assess the performance of NewAthena's Wide Field Imager. We created a supermassive black hole (SMBH) light-cone, spanning 10 deg^2, with corrections to account for the limited resolution of the simulation and X-ray properties derived in post-processing. The resulting catalogue reveals a $\sim 5\times$ overabundance of faint AGN compared to current X-ray constraints, an inconsistency potentially resolved by invoking a higher Compton-thick (CTK) fraction and intrinsic X-ray weakness, as suggested by recent *JWST* findings. An end-to-end survey simulation using SIXTE predicts ∼250 000 AGN detections, including ∼20 000 at $z > 3$ and 35 in the epoch of reionization (EoR; $z > 6$); notably, only AGN with $L_X > 10^{43.5}$ erg s^{-1} are detectable at $z > 6$. The analysis also forecasts a significant population of detectable CTK AGN, even beyond $z > 4$. These findings suggest X-ray observations will, for the first time, probe a significant AGN population in the EoR, offering new insights into SMBH growth. They also provide key input for refining NewAthena's mission design and optimizing its survey strategy.

Key words: telescopes – surveys – galaxies: active – galaxies: high-redshift – quasars: supermassive black holes – X-rays: galaxies.

1 INTRODUCTION

One of the major goals of contemporary astrophysics is to unravel the complex processes governing galaxy formation and evolution. Among the most significant discoveries is the phenomenon of active galactic nuclei (AGNs), a luminous and compact source that can outshine the emission from the entire host galaxy. Currently, it is widely established that this emission arises from the accretion of matter into the supermassive black hole (SMBH) present at the centre of every massive galaxy (e.g. Kormendy & Richstone 1995; Volonteri 2010).

Given the prevalence of SMBHs within galaxies, it is plausible that any presently inactive galaxy may have previously hosted an AGN. Furthermore, since the energy emitted by the AGN can exceed that emitted by its host, the coupling of this energy, through feedback mechanisms, can significantly impact the host (e.g. Fabian 2012; Morganti 2017). Moreover, we have evidence of co-evolution and self-regulation between the SMBH and the host, in the ubiquity of the scaling relations between the mass of the SMBH and galactic properties, such as the $M_\bullet - \sigma$ relation (Kormendy & Ho 2013; see also D'Onofrio, Marziani & Chiosi 2021 for a recent review).

For these reasons, it is crucial to understand the growth of SMBHs as a function of redshift (e.g. Yang et al. 2018) and the duty cycle of AGN (i.e. the fraction of time a galaxy hosts an AGN). Achieving this requires a detailed demographic analysis of AGN populations, beginning with a complete and systematic census of their properties.

The X-ray regime is commonly favoured for AGN census (e.g. Brandt & Alexander 2015), due to several advantages. First, AGN X-ray emission typically surpasses that of stellar processes within the

★ E-mail: nunocovas27@gmail.com

host, ensuring that X-ray surveys maintain a high purity in contrast to infrared (IR) surveys. Moreover, hard X-rays are relatively unaffected by obscuration, rendering X-ray surveys more complete and unbiased compared to optical surveys (e.g. Hickox & Alexander 2018). Finally, X-ray emission is a good tracer of accretion in AGN because it originates from the innermost parts of the accretion disc around the SMBH (e.g. Jovanović & Popović 2009).

While current X-ray surveys have been indispensable to probe the properties of AGN, they have a few limitations. We currently lack a complete and unbiased knowledge of the faintest sources, such as high-redshift ($z > 3$) AGN (Pouliasis et al. 2024) or the Compton-thick (CTK) population (i.e. AGN with a line-of-sight column density, $N_{\rm H} > 1.5 \times 10^{24}\,{\rm cm}^{-2}$). Although current facilities such as *XMM–Newton* or *Chandra* have been used to place some constraints on these populations, the detailed characterization of the fainter AGN population will require telescopes with significantly better photon collecting capacity.

These observational limitations highlight the need for next-generation X-ray observatories, as recognized in ESA's Cosmic Vision program 'The Hot and Energetic Universe' (Nandra et al. 2013), which led to the selection of ATHENA as the second Large-class Mission (L2). ATHENA combines a large effective area, high angular resolution, and a wide field of view (FOV). Its original design featured a single grazing incidence telescope with a 12 m focal length (Willingale et al. 2013), an effective area of 1.4 m^2 at 1 keV, a 5 arcmin on-axis half energy width (HEW), an FOV exceeding 40 arcmin × 40 arcmin, and a homogeneous point spread function (PSF). This breakthrough is possible with the silicon pore optics technology (Collon et al. 2017; Barrière et al. 2022), which ensures a high ratio of collecting area to mass while maintaining the required angular resolution. The mission incorporates two instruments: the Wide Field Imager (WFI; Antonelli et al. 2024) and the X-ray Integral Field Unit (X-IFU; Barret et al. 2018, 2023). The WFI is a silicon detector using depleted p-channel field effect transistor (DEPFET) active pixel sensor technology, with a 40 arcmin × 40 arcmin FOV, a 0.2–12 keV spectral range, 80–170 eV energy resolution, and an 80 μs time resolution. The X-IFU is a cryogenic spectrometer with an unprecedented 2.5 eV energy resolution at 7 keV and a 5-arcmin FOV. The groundbreaking potential of ATHENA was demonstrated by comprehensive end-to-end simulations by several groups. Marchesi et al. (2020) assessed the performance of ATHENA's WFI survey concerning high-redshift AGN, while Zhang et al. (2020) conducted a similar study focusing on extended sources.

In 2022, ATHENA's development paused due to cost concerns. ESA later conceived NewAthena (Cruise et al. 2024), a rescoped concept retaining flagship status and most of ATHENA's capabilities, targeting adoption by 2027 and a 2037 launch. NewAthena features a smaller mirror with an effective area of ∼1 m^2 at 1 keV and a broader PSF with a better-than 9 arcmin on-axis HEW. The WFI largely maintains its original specifications, while the X-IFU will have a reduced FOV (4 arcmin × 4 arcmin) and a 4 eV energy resolution at 7 keV. This reconfiguration led to a reduction in sensitivity and resolution, consequently, it is essential to revisit the end-to-end simulations to evaluate how these changes affect the mission's outcomes and maximize the scientific return within these constraints.

A fundamental ingredient of such simulations pertains the modelling of the input AGN, especially in the poorly constrained regions of the parameter space. Several approaches exist, such as extrapolations of the X-ray luminosity function (XLF; Marchesi et al. 2020). However, these methods are not physically motivated and have limited constraints at high redshift. Consequently, complementary methods should be considered.

Cosmological hydrodynamical simulations (HDS) are particularly insightful because they model galaxy formation by solving the equations of gravity and hydrodynamics in a cosmological context, tracing the properties of dark matter (DM), gas, and stars in discrete resolution elements (see Somerville & Davé 2015 and Vogelsberger et al. 2020 for reviews), albeit at a significant computational cost. Despite their strengths, they rely on subgrid prescriptions to represent unresolved processes, such as SMBH accretion and AGN feedback, that have been instrumental to the success of these models in reproducing observations (see Di Matteo, Angles-Alcazar & Shankar 2023 for an extensive review on the role of SMBHs in recent cosmological simulations).

By simulating galaxy formation from physically motivated prescriptions, these models offer invaluable insights into AGN in the high-redshift universe, where observations are limited, making them ideal for creating mock catalogues to test NewAthena. Moreover, they provide direct access to SMBH properties, such as masses, accretion rates, and AGN clustering. This framework has been extensively used in the literature, to provide predictions for surveys such as the XMM-XXL survey with *XMM–Newton* (Koulouridis et al. 2018) or the extended ROentgen Survey with an Imaging Telescope Array (eROSITA) surveys (Biffi, Dolag & Merloni 2018; Comparat et al. 2019). Previous work also ventured into making predictions for ATHENA, as evidenced by Habouzit et al. (2021), albeit their approach primarily involved analytical predictions (akin to Amarantidis et al. 2019), without delving into an end-to-end simulation of the survey.

In this work, we leverage a cosmological simulation of galaxy formation to create an X-ray mock catalogue of AGN, and simulate the X-ray sky to make quantitative predictions on the performance of NewAthena's WFI survey. Our focus is on evaluating its capability to 'Measure the space density of AGN that drive SMBH growth up to the Epoch of Reionization.'[1]

The paper is organized as follows: Section 2 describes the methodology to create the mock catalogue and the observational comparisons used for validation. Section 3 presents SIXTE, the software used to simulate the mock observations, discusses the simulation strategy, and outlines the detection process. In Section 4, we present the results that are discussed in Section 5. We present our conclusions in Section 6. We assume a flat Lambda-cold dark matter cosmology with $H_0 = 67.4\ {\rm kms}^{-1}{\rm Mpc}^{-1}$, $\Omega_{\rm m} = 0.315$, and $\Omega_\Lambda = 0.685$ (Planck Collaboration VI 2020).

2 A COSMOLOGICAL AGN MOCK CATALOGUE

2.1 ILLUSTRISTNG

In this work, we adopted the ILLUSTRISTNG cosmological simulation (Nelson et al. 2021), a state-of-the-art HDS. It consists of three flagship runs, in three different cosmological volumes: TNG50, TNG100, and TNG300, corresponding to box lengths of 50, 100, and 300 cMpc, respectively. We chose the TNG300 box, which is large enough to provide a statistically robust sample of AGN, essential for studying high-redshift AGN. TNG300 has a volume of approximately $(300\,{\rm cMpc})^3$, achieves a DM mass resolution of $M_{\rm DM} = 5.9 \times 10^7\,{\rm M}_\odot$, and a baryonic matter mass resolution of $M_{BM} = 1.1 \times 10^7\,{\rm M}_\odot$.

[1] https://www.the-athena-x-ray-observatory.eu/en/unveiling-universe-x-rays

ILLUSTRISTNG builds upon the success of the original ILLUSTRIS simulation (Nelson et al. 2015), incorporating significant improvements in the numerical implementation, and an updated physical model. The TNG model introduces magnetic fields, refines the model for the galactic winds, and updates the stellar evolution and chemical enrichment processes (see Pillepich et al. 2018a for a detailed description and comparison with ILLUSTRIS). The model also includes a new prescription for SMBH growth and dual mode AGN feedback (Weinberger et al. 2017). This new model alleviates some of the observational tensions in ILLUSTRIS and produces more realistic galaxy populations (e.g. Marinacci et al. 2018; Naiman et al. 2018; Nelson et al. 2018; Springel et al. 2018; Pillepich et al. 2018b).

The new SMBH model places seed SMBHs, with a mass of $1.2 \times 10^6\,M_\odot$, in DM haloes with a mass greater than $7.4 \times 10^{10}\,M_\odot$, that do not contain an SMBH. Once seeded, these SMBHs grow through merging or Bondi–Hoyle accretion,[2] given by

$$\dot{M} = \frac{\alpha 4\pi (GM)^2 \rho}{(c_s^2 + v_\infty^2)^{3/2}}, \tag{1}$$

where $\dot{M}$ is the accretion rate, G is the gravitational constant, M is the mass of the SMBH, ρ is the local gas density, c_s is the local sound speed, α is the boost factor that takes into account the unresolved interstellar medium (ISM), and v_∞ is the gas speed around the SMBH. In the TNG model, $\alpha = 1$, $v_\infty = 0$, and the accretion is capped at the Eddington limit:

$$\dot{M}_{\rm Edd} = \frac{4\pi G M m_p}{\epsilon_r \sigma_T c}, \tag{2}$$

where m_p is the proton mass, ϵ_r is the radiative efficiency, which ILLUSTRISTNG adopts as 0.2, and σ_T is the Thompson scattering cross-section.

The model implements two modes of AGN feedback: thermal and kinetic modes. If the Eddington ratio ($\lambda = \frac{\dot{M}}{\dot{M}_{\rm Edd}}$) exceeds a value of $\min[0.002(\frac{M}{10^8 M_\odot})^2, 0.1]$, thermal energy is injected into the neighbouring gas particles at a rate given by $\epsilon_{f,\rm high}\epsilon_r \dot{M}c^2$. If the Eddington ratio is below this value, kinetic energy is injected into the gas at regular intervals of time, in the form of a wind oriented along a random direction. The energy injected is given by $\epsilon_{f,\rm low}\dot{M}c^2$ and the coupling efficiencies $\epsilon_{f,\rm high}$ and $\epsilon_{f,\rm low}$ are free parameters of the model. For further details, the reader is referred to Weinberger et al. (2017, see also Weinberger et al. 2018 and Terrazas et al. 2020 for a detailed exploration of the impact of this improved feedback model).

Before attempting to create a mock catalogue from this simulation, it is insightful to verify whether there is enough data to cover the relevant redshift range. To do so, one of the axes of the box must be converted to a dimension in redshift, by inverting the following equation:

$$d_c(z) = \frac{c}{H_0}\int_{z_1}^{z_2} \frac{{\rm d}z'}{\sqrt{\Omega_m(1+z')^3 + \Omega_\Lambda}}, \tag{3}$$

where $d_c(z)$ is the comoving distance in the redshift interval between z_1 and z_2, H_0 is the *Hubble* constant, and Ω_m, Ω_Λ are the matter and dark energy density parameters. With this prescription, each of the 100 snapshots from TNG300 can be assigned to a specific redshift interval, centred on the fiducial redshift of the snapshot, as illustrated in Fig. 1.

[2]Spherically symmetric accretion by a point source moving at a steady speed through a uniform gas cloud (Edgar 2004).

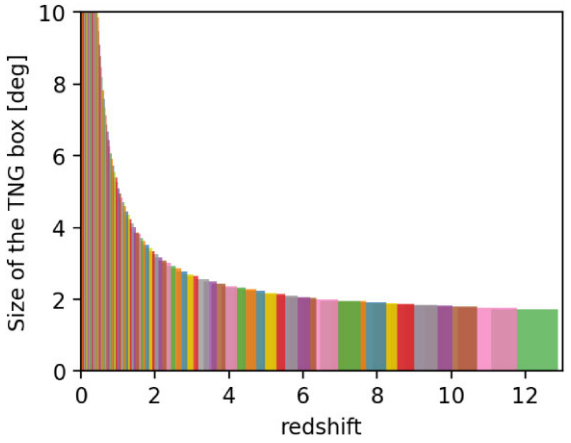

Figure 1. Graphical representation of the angular size as a function of redshift in TNG300. The *x*-axis shows snapshot redshifts, and the *y*-axis indicates the projected angular box size (300 cMpc) in degrees. Bar widths correspond to the redshift range of each box, with alternating colours for clarity. Due to the large number of snapshots, the redshift ranges of all boxes overlap significantly.

2.2 Building the light-cone

The raw output of the simulation are discrete snapshots of the simulated box, in the comoving rest frame (i.e. removing the effect of cosmological expansion). These cannot be directly used as input for the end-to-end simulations; instead, a continuous light-cone must be created, which we have implemented in the following way (Amarantidis 2021):

(i) For each snapshot, all SMBH particles are retrieved.[3] Each particle carries information about its identification, position, BH mass, accretion rate, nearby gas density, the total mass of the particle (BH+gas reservoir), and the mass of the host halo.

(ii) Due to the redshift overlap in the boxes (see Fig. 1), care must be taken to not duplicate the SMBH in overlapping regions. Therefore, for each snapshot, we only keep the sources in a limited slice. The width of this slice is calculated as the difference between the comoving distances at the redshift of the current snapshot and at the redshift of the following snapshot. The slice is then sampled from a random position in the box.

(iii) Since the simulation evolves the same sources forward in time, their positions remain roughly consistent across snapshots. To avoid biasing the catalogue, each box is rotated $\pm 90^\circ$ around a random axis. Although these rotations helped mitigate bias, some circular artefacts persisted. To address this, a random translation of the box centre is also applied, effectively removing the remaining artefacts, while preserving the structure and correlations between the sources in the slice.

(iv) Since the snapshots are discrete, some processing is necessary to assign a different redshift to each source, ensuring a continuous light-cone. First, the redshift of the snapshot is used to calculate a comoving distance, using equation (3), then the radial coordinate of each particle is added to this value, and the resulting distances are converted into redshifts for each particle by inverting equation

[3]No mass cut has been applied to the catalogue, therefore the newly- eeded SMBHs are included in the analysis. However, due to their low accretion rate, they do not contribute significantly to the results and are mainly a source of unresolved background.

(3). Each of these redshifts is then used to calculate a scale factor[4,5] that converts the transverse coordinates, in ckpc, to the projected sky coordinates right ascension and declination, in arcminutes.

(v) The fixed dimension of the simulated box, 300 cMpc, limits the angular size of the light-cone that can be constructed from it. The high-redshift scale factor, at $z = 12$, limits the light-cone to a projected angular size of 1.6 deg, as plotted in Fig. 1, corresponding to an area of 2.5 deg^2[6] Considering this, four unique light-cones were created from replications of the TNG300 box. Thus, the final light-cone covers an area of simulated sky equivalent to 10 deg^2 in a redhsift range from 0 to 12.

2.2.1 *Resolution correction*

In addition to the physical model, there are two critical factors in cosmological simulations: the volume of the box and the resolution of the particles. Large volumes are necessary to simulate a representative universe, with the rarest and most massive AGN; a high resolution is necessary to ensure accurate model results. There is always a trade-off between these parameters; a larger volume of the simulated box necessitates a lower resolution to maintain computational feasibility. The ILLUSTRISTNG simulations also follow this general trend: the TNG300-1 box has a volume 27 times larger than the volume of TNG100-1, however, the spatial and mass resolutions are lower by a factor of 2 and 8, respectively.

As discussed in appendix B of Weinberger et al. (2018), the resolution has a significant impact on the properties of galaxies and SMBH. The accretion rates and masses, as a function of the host halo mass, are systematically lower, compared to the high-resolution simulation. This is especially important for SMBH in lower mass haloes ($< 10^{12}\,M_\odot$), since the haloes are resolved by few particles and the SMBH are not in the self-regulating regime (kinetic feedback mode). This greatly impacts the bright end of the XLF, and it is critical for high-redshift predictions, where most of the SMBH exists in these haloes.

To study model convergence, the TNG project repeated all flagship runs at a lower resolution; TNG100-2 has the same volume and initial conditions as TNG100-1, but the same resolution as TNG300-1. Comparing these simulations allows one to account for the impact of the lower resolution. This has been done in Pillepich et al. (2018b), where the authors determined simple corrections for the stellar masses and star formation rates of TNG300-1. Motivated by that work, we derived corrections for the distributions of the Eddington ratio of the SMBH. The details are in Appendix A.

The results of these corrections are illustrated by Fig. 2, which plots the histograms of the Eddington ratio distributions of TNG100-1 and TNG100-2, as well as the corrected distribution, TNG100-2c. The figure shows that the high- and low-resolution simulations produce different distributions (Fig. 2, red and green histograms, respectively) and the corrections are successful as the corrected distribution of Eddington ratios (blue histogram) is similar to the high-resolution simulation (red histogram). The K-S test has a p-value of 0.27 and 0.79 at $z = 0$ and 5, respectively, therefore the TNG100-1 and TNG100-2-c distributions are statistically indistinguishable. Comparing TNG100-2 and TNG100-2-c, at $z = 0$, the high-lambda

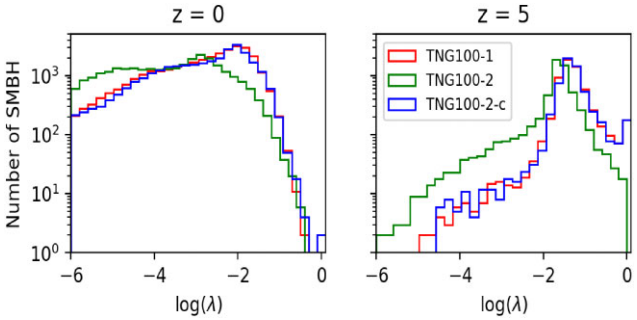

Figure 2. Histograms of log(λ) distributions at $z = 0$ (left) and $z = 5$ (right) for TNG100-1 (red), TNG100-2 (green), and the corrected TNG100-2-c (blue). The y-axis (logarithmic scale) shows frequencies, highlighting the similarity between TNG100-1 and TNG100-2-c at both redshifts.

end of the distribution is similar; however, this is not the case at $z = 5$, where the correction considerably increases the number of SMBH accreting at the Eddington limit. This has important implications regarding the X-ray luminosity of these AGN and consequently, their detectability with future X-ray observatories such as NewAthena.

2.3 X-ray properties

ILLUSTRISTNG does not provide X-ray properties for the AGN; therefore, these are determined in post-processing, following several models and empirical assumptions.

2.3.1 *X-ray luminosity*

The model adopted to calculate the bolometric luminosity assumes two distinct modes of accretion: a Shakura–Sunyaev thin disc for high Eddington ratio AGN (Shakura & Sunyaev 1973), and an advection dominated accretion flow (ADAF) for low Eddington ratio AGN (e.g. Yuan & Narayan 2014). For ADAF, the radiative efficiency depends on the Eddington ratio (Mahadevan 1997; Churazov et al. 2005; Hirschmann et al. 2014), resulting in a decrease of this value compared to the thin disc model. The reader is referred to Yuan & Narayan (2014) for a review on ADAF and other hot accretion flows. This model can be parametrized in the following way:

$$L_{\rm Bol} = \begin{cases} \epsilon_r \dot{M} c^2 & \text{if } \lambda >= 0.1 \\ \dfrac{0.2}{\alpha^2} \lambda \epsilon_r \dot{M} c^2 & \text{if } \lambda < 0.1 \end{cases} \quad (4)$$

where $\dot{M}$ is the accretion rate, $\dot{M}_{\rm Edd}$ is the accretion rate at the Eddington limit, $\lambda = \frac{\dot{M}}{\dot{M}_{Edd}}$ is the Eddington ratio, $\epsilon_r = 0.08$ is the radiative efficiency we assume (see Section 2.4), c is the speed of light, and α is the viscosity parameter.

This model is very similar to the one adopted in previous work with ILLUSTRISTNG (Weinberger et al. 2018; Habouzit et al. 2019, 2021). The main difference is the numerical prefactor of the ADAF. Previous works assumed a constant factor of 10, to ensure continuity between the branches of the function; however, as explained by Griffin et al. (2019), this prefactor depends on the radius of the innermost stable circular orbit, which depends on the spin of the SMBH. Since ILLUSTRISTNG does not track this quantity, we model the ADAF following equation (58) of Mahadevan (1997), which assumes canonical values for the unconstrained parameters, and adopt $\alpha = 0.3$, consistent with the findings of Liu & Taam (2013).

After the bolometric luminosities were calculated, we determined the X-ray luminosities assuming a bolometric correction, $K_{\rm X} = \frac{L_{\rm Bol}}{L_{\rm X}}$.

[4]Using the function kpc_comoving_per_arcmin from the astropy.cosmology package

[5]https//docs.astropy.org/en/stable/cosmology/index.html

[6]The actual size is 1.7 deg, however, the light-cone is further limited to ensure some margin, for the translations of the box centre.

We adopt the hard X-ray (2–10 keV) corrections from Duras et al. (2020), since these are the most up-to-date bolometric corrections for X-ray, and are valid in a range of 7 dex in bolometric luminosity:

$$K_X(\lambda) = 7.51\left(1+\left(\frac{\lambda}{0.05}\right)^{0.61}\right). \quad (5)$$

To model the scatter, due to the variability, which is not resolved by these simulations (Habouzit et al. 2021), as well as the intrinsic X-ray weakness in some AGN populations (Pu et al. 2020; Laurenti et al. 2022; Lyu et al. 2024; Maiolino et al. 2024), the value of the bolometric correction is randomly sampled from a Gumbel distribution, centred on the relation from Duras et al. (2020), with a width of 0.5 dex (Habouzit et al. 2021).

Finally, these X-ray luminosities are converted into X-ray fluxes, using the formula:

$$F_X = \frac{L_X}{4\pi(d(1+z))^2 K(z)}, \quad (6)$$

where L_X is the 2–10 keV X-ray luminosity, z is the redshift of the AGN, d is the comoving distance at that redshift, and $K(z)$ is the K-correction. The K-corrections are calculated using the spectral templates (see Section 2.3.3) assumed for each AGN.

2.3.2 *Obscuration model*

X-ray AGN are typically obscured by gas within the line of sight, due to the photoelectric absorption, at energies below 10 keV, or Compton scattering at higher energies. Therefore, we must assume an obscuring column density, N_H, for each AGN (Hickox & Alexander 2018). The model we adopted is similar to the radiation-lifted torus model developed by Buchner, Schulze & Bauer (2017) and Buchner & Bauer (2017). It comprises three components: CTK obscuration, nuclear Compton thin obscuration (CTN), and CTN obscuration from the host.

Regarding CTK obscuration, despite substantial efforts by multiple teams to directly constrain it through X-ray surveys (e.g. Lanzuisi et al. 2018; Georgantopoulos & Akylas 2019; Lambrides et al. 2020; Torres-Albà et al. 2021; Laloux et al. 2022; Carroll et al. 2023; Yan et al. 2023) significant uncertainties and discrepancies persist. A complementary approach to quantifying this heavily obscured AGN population involves population synthesis models that fit the cosmic X-ray background (CXB) (e.g. Gilli, Comastri & Hasinger 2007; Ueda et al. 2014) and estimate the CTK fraction. The most recent model of this kind, developed by Ananna et al. (2019), provides improved consistency with X-ray observational constraints and predicts an average CTK fraction of 50 per cent in the local universe.

However, the most recent observations with the *JWST* find many AGN (candidates) that are remarkably X-ray weak (Lyu et al. 2024; Maiolino et al. 2024) and one of the leading explanations for this phenomenon is a significant increase in the CTK fraction with redshift, for intermediate-luminosity ($L_{Bol} < 10^{11}\,L_\odot$) AGN. Considering this, our model assumes a CTK fraction parametrized as:

$$F_{CTK} = 0.4 + 0.5\frac{1-e^{-z}}{1+e^{\log L_X - 44}}, \quad (7)$$

with N_H drawn randomly from a loguniform distribution, between 10^{24} and 10^{26} cm^{-2}. For further discussion on these assumptions, the reader is referred to Section 2.4

Unlike the CTK obscuration, the CTN obscuration is much better constrained, with several works finding an evolution with redshift and an anticorrelation with the luminosity (e.g. Ueda et al. 2014; Peca et al. 2023), therefore, most obscuration models assume an explicit luminosity dependence for this fraction. However, the work by the BAT AGN spectroscopic survey (BASS) team on the radiation-regulated growth model for AGN (Ricci et al. 2017b, 2022, 2023; Ananna et al. 2022) shows that, in the local universe, the main driver of nuclear obscuration is the Eddington ratio. For this reason, the nuclear CTN fraction is calculated based on a sigmoid fit to the X-ray covering fraction in fig. 3 of Ricci et al. (2023):

$$F_{CTN} = 0.6\frac{10^{-1.21(x+1.525)}}{1+10^{-1.21(x+1.525)}} + 0.25, \quad (8)$$

where $x = \log_{10}(\lambda)$, with λ the Eddington ratio and N_H is chosen randomly from a loguniform distribution, between 10^{22} and 10^{24} cm^{-2}. Although this relation was derived using local AGN, we assume its validity for all z (see Jun et al. 2021 for a discussion on the $N_H - \lambda$ relation at higher z).

The last component of the model is the obscuration by the host. Although this component might not be very important at low z, since it cannot exceed a column density of 10^{22} cm^{-2}, recent works (e.g. Circosta et al. 2019; D'Amato et al. 2020; Gilli et al. 2022; Signorini et al. 2023) show that this might be the dominant source of obscuration at high z, even reaching CTK column densities. ILLUSTRISTNG is an HDS, therefore, the obscuration from the host could be measured by ray-tracing of the gas particles, the approach followed by Buchner & Bauer (2017); however, that is beyond the scope of this work and instead a simplified model, based on the work by Gilli et al. (2022) is used.

The obscuration from the host galaxy is modelled using a log-normal distribution with an average column density of $10^{21}(1+z)^{3.3}$ cm^{-2} and a standard deviation of 0.5 dex. In addition, a constant host covering fraction of 40 per cent is assumed. Given the significant uncertainty in the redshift evolution of the host covering fraction, we adopted the average value of the sample by Buchner & Bauer (2017).

After using the model to determine the column density for each AGN, the values are binned and used, with the spectral templates (see Section 2.3.3), to calculate the observed flux in the soft (0.5–2 keV) and hard (2–10 keV) bands.

2.3.3 *AGN spectral templates*

To model X-ray AGN, some spectral shape must be assumed for each source. The templates used in this work, shown in Fig. 3, were

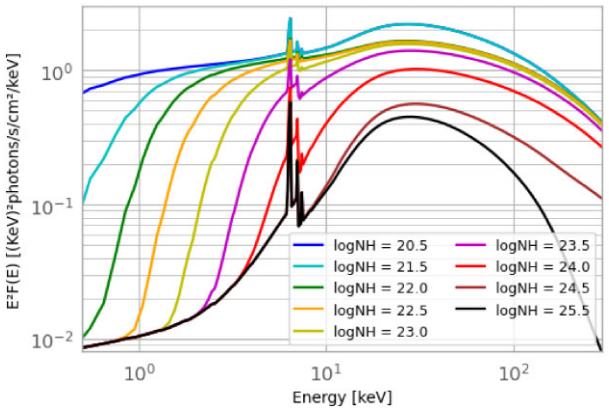

Figure 3. Example spectral templates employed for AGN in the mock catalogue, at $z = 0$, delineated across various logN_H values as depicted in the legend. All spectra have $\Gamma = 1.9$.

created using PyXspec (Gordon & Arnaud 2021), a python interface for the xspec software (Arnaud 1996).

In xspec nomenclature, three different types of models are employed, according to three regimes of obscuration:

$$phabs * \big(c * zcutoffpl + zphabs * cabs * (pexmon)\big), \quad \log N_H < 22 \tag{9}$$

$$phabs * \big(c * zcutoffpl + zphabs * cabs * (zcutoffpl) + pexmon\big), \quad 22 \leq \log N_H < 25 \tag{10}$$

$$phabs * \big(c * zcutoffpl + pexmon\big), \quad \log N_H \geq 25 \tag{11}$$

These spectral templates model key features commonly observed in X-ray spectra of AGN, such as a primary X-ray continuum, a reflection component, and an unabsorbed scattered component (Ueda et al. 2014; Ricci et al. 2017a; Ananna et al. 2019).

The primary X-ray continuum is the result of the Comptonization of the thermal photons from the accretion disc, occurring in the hot corona above the disc. More specifically, the thermal photons undergo inverse Compton scattering from the energetic electrons present in the corona, which increases their energy and prompts a cascade of more energetic scattering events. This results in a power-law spectrum, with a slope given by the photon index, Γ, and an exponential cut-off at high energy, since eventually the photons reach the energy of the electrons and the energy transfer becomes inefficient (Done 2010).

Therefore, the primary continuum emission is modelled as a cut-off power law, with a cut-off energy, $E_c = 200$ keV, close to the mean value found in Ricci et al. (2017a), with a Kaplan–Meier estimator; this value is also supported by the nuclear spectroscopic telescope array (NuSTAR) observations (e.g. Akylas & Georgantopoulos 2021). Photoelectric absorption and Compton scattering are taken into account by the zphabs and cabs models, respectively. Both models assume the same N_H value.

This primary emission can then be transmitted, reflected, or scattered. The reflected component is modelled by Pexmon (Nandra et al. 2007), which assumes that the primary emission is reflected by the accretion disc. This model also takes into account self-consistently generated fluorescence lines, namely the Fe K_α, Fe K_β, Ni K_α, and Fe K_α Compton shoulder. Pexmon assumes a cut-off power law, with the same shape and magnitude as the primary emission, the inclination angle of the accretion disc is fixed at 30°, while the reflection strength is $R = 0.83$, for the unobscured AGN, and $R = -0.37$ for the obscured AGN. These are the mean values of the reflection strength of Ricci et al. (2017a) when the upper and lower limits of all AGN are taken into account. These measurements are also consistent within 1σ with the values of Akylas & Georgantopoulos (2021) for unobscured AGN, with NuSTAR.

It is important to note that in our assumption, all obscuration with a column density below $\log N_H < 22$ is attributed to the host. Consequently, in equation (9), obscuration is accounted for in the reflected component. Conversely, in equation (10), the reflected component remains unobscured. This approach is consistent with the templates presented in Marchesi et al. (2020), Ricci et al. (2017a), and Ueda et al. (2014).

The scattered component is modelled by a cut-off power law with the same shape and magnitude as the primary continuum, with a scattered fraction of 1 per cent, the mean value of Ricci et al. (2017a). Although a recent investigation by Gupta et al. (2021) identified a correlation between the scattered fraction and the column density among obscured sources, we opted for a simplified approach, assuming the mean value of their *Swift*–BAT (Burst Alert Telescope) sample in all spectral templates.

The *phabs* model takes into account the local obscuration from the Milky Way, with an $N_H = 1.8 \times 10^{20}$ cm^{-2} Marchesi et al. 2020). All other parameters, not explicitly mentioned, were left to their default values. The photon indices were randomly chosen from a normal distribution with a mean value of $\Gamma = 1.9$ and a standard deviation of $\Delta\Gamma = 0.15$ (Gilli et al. 2007). These spectral templates cover a redshift range between 0 and 10, with a step of $\Delta z = 0.1$; a photon index range between 1.7 and 2.1, with a step of $\Delta\Gamma = 0.1$ and a $\log N_H$ range between 20.5 and 25.5, with a step of 0.5. Following Marchesi et al. (2020), the spectra with $\log N_H > 25$ are modelled as reflection-dominated spectra, without a transmitted component. The mock catalogue has a flux limit of 10^{-30} erg s^{-1}cm^{-2}.

2.4 Mock catalogue validation

We tested the mock catalogue against available constraints, namely the obscured fractions, the cumulative number counts, and the CXB flux.

Fig. 4 compares the obscured fractions in the mock catalogue with several measurements from the literature. The upper panels plot the CTN fraction, defined as:

$$F_{CTN}(z) = \frac{N(22 <= \log(N_H) <= 24)}{N(\log(NH) <= 24)}, \tag{12}$$

as a function of the hard X-ray luminosity (2–10 keV), for redshift ranges $0 < z < 1$ (left plot) and $1 < z < 2$ (right plot) and compare the mock catalogue with the measurements from Peca et al. (2023). Despite not assuming a direct dependence on the luminosity, the adopted model successfully reproduces the observed anticorrelation at low z. The bottom-left panel plots the CTN fraction as a function of z, for two luminosity ranges, $43 < \log(L_X) < 44$ (blue) and $44 < \log(L_X) < 45$ (red), again the mock catalogue is compared with the measurements from Peca et al. (2023). There is good agreement in the results for $z < 2$, however, for higher z, the CTN fraction flattens at 65 per cent, while the best fits by Peca et al. (2023) continue to increase. It should be noted, however, that this flattening is consistent with previous works (see fig. 13 in Peca et al. 2023; see also Aird et al. 2015; Buchner et al. 2015; Ananna et al. 2019) and remains broadly consistent within the uncertainties given that the fit for $\log L_X = 43$–44 is extrapolated beyond $z = 3$.

The bottom-right panel of Fig. 4 plots the obscured fraction, defined as

$$\text{Obscured fraction}(z) = \frac{N(23 <= \log(N_H) <= 26)}{N(\log(NH) <= 26)}, \tag{13}$$

for a redshift range $0 < z < 6$ and compares it with several measurements from the literature. This fraction seems to overestimate the constraints, however, this is not unexpected as current surveys are strongly biased against AGN with $N_H > 10^{25}$ cm^{-2}. If these AGN are excluded and the obscured fraction redefined, the agreement with the observations improves remarkably, further validating our assumptions regarding the CTK fraction. Overall, the obscuration model seems to comply with the observations.

The next step in the validation process is to verify the cumulative number counts in the mock catalogue. Fig. 5 plots the cumulative number counts in the hard X-ray band (2–7 keV) and compares them with the measurements in Chandra Deep Field South-7Ms (CDFS-7Ms; Luo et al. 2016) and Chandra Deep Wide Field South (CDWFS; Masini et al. 2020). In the left plot of Fig. 5, the number counts

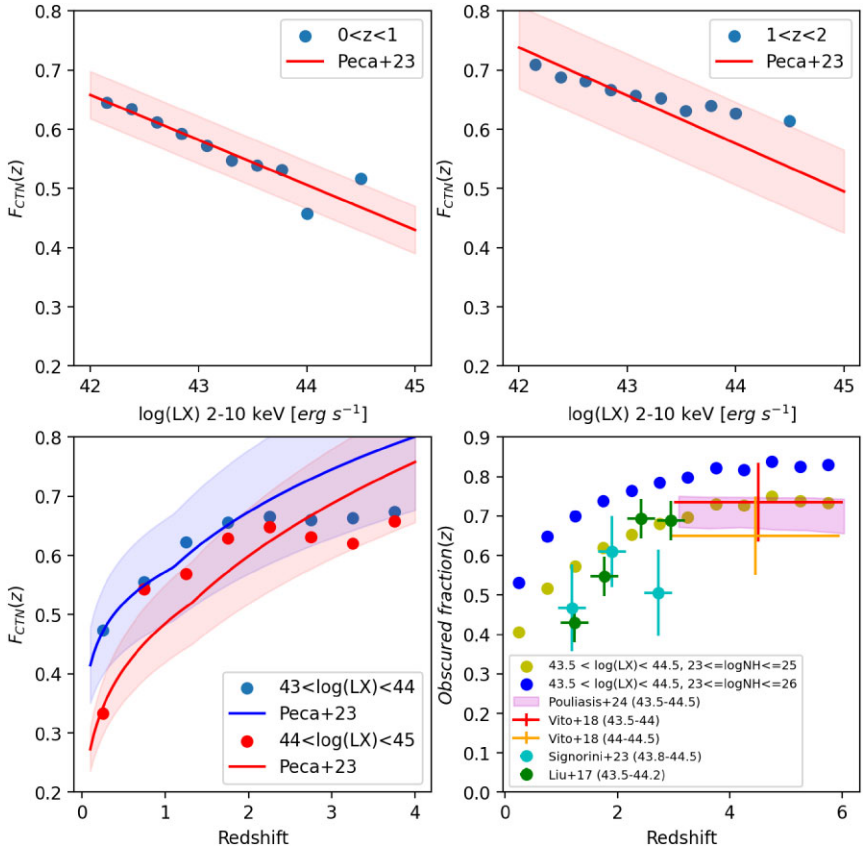

Figure 4. Top-left panel: the CTN fraction, $F_{\rm CTN}(z)$, defined in equation (12), in a redshift range $0 < z < 1$, is presented (blue dots) and compared to the recent work by Peca et al. (2023, red line fit and uncertainty band). Top-right panel: the same as the top-left panel, but for a redshift range $1 < z < 2$. Bottom-left panel: the evolution of the $F_{\rm CTN}(z)$ with redshift, for two luminosity ranges: $43 < \log(L_{\rm X}) < 44$ (blue points) and $44 < \log(L_{\rm X}) < 45$ (red points). The data are also compared with fits and uncertainty bands from Peca et al. (2023). Bottom-right panel: the obscured fraction, now defined by equation (13) (blue dots) or with $\log(N_{\rm H}) < 25$ (yellow dots), for a luminosity range of $43.5 < \log(L_{\rm X}) < 44.5$, is presented as a function of redshift and compared with several works in the literature, namely: Pouliasis et al. (2024), Vito et al. (2018), Signorini et al. (2023), and Liu et al. (2017).

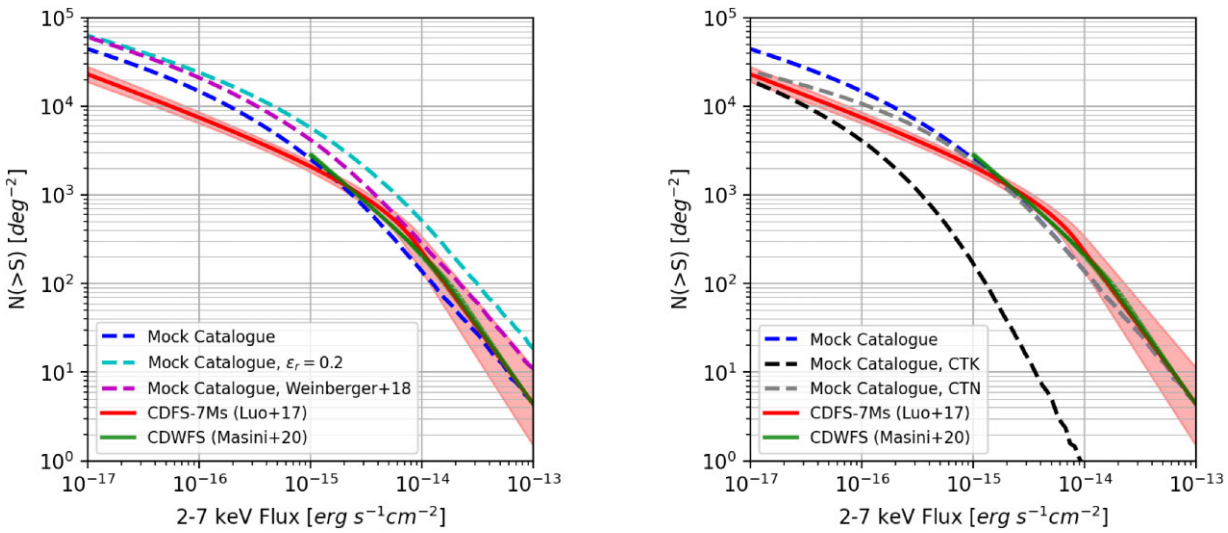

Figure 5. Comparison of cumulative AGN number counts as a function of 2–7 keV flux (erg $s^{-1}cm^{-2}$) from the mock catalogue (blue) with observational data sets. Flux is derived from 2–10 keV flux using a power-law model ($\Gamma = 1.4$). The red line shows the CDFS-7Ms survey fit (Luo et al. 2016), and the green line represents CDWFS data (Masini et al. 2020), with corresponding confidence intervals (red/green bands). Predictions using $\epsilon_r = 0.2$ (cyan) and the bolometric luminosity model (Weinberger et al. 2018, magenta) are included. The second panel partitions counts into CTK and CTN categories.

show reasonable agreement above 10^{-15} erg s^{-1}cm^{-2}. Below this flux the faint-end slope differs, resulting in an excess of faint AGN by a factor of ∼2, compared to CDFS-7Ms. These number counts are corrected for the incompleteness of the survey, which critically depends on the obscuration distribution of the AGN, that is not adequately constrained by Luo et al. (2016, see Lambrides et al. 2020 for further details). Since their selection is biased against CTK AGN, this could explain the disagreement at the faintest fluxes.

Inspecting now the constraints of the CXB, the total flux in the hard band (2–10 keV) is 2.16×10^{-11} erg s^{-1}cm^{-2}deg^{-2}, while the total flux in the soft band (0.5–2 keV) is 0.88×10^{-11} erg s^{-1}cm^{-2}deg^{-2}. Cappelluti et al. (2017) measure the CXB spectrum and find total extragalactic fluxes of $(2.034 \pm 0.005) \times 10^{-11}$ erg s^{-1}cm^{-2}deg^{-2} and $(0.76 \pm 0.01) \times 10^{-11}$ erg s^{-1}cm^{-2}deg^{-2} in the hard (2–10 keV) and soft (0.5–2 keV) bands, respectively. The mock catalogue and this measurement differ by 6 per cent and 16 per cent in the hard and soft bands, respectively, which is within the calibration uncertainties, that could reach 20 per cent (Marchesi et al. 2020). Given their uncertainties, the flux values from our mock catalogue agree with these measurements.

Cappelluti et al. (2017) also present results for the unresolved CXB, after removing all sources detected by Civano et al. (2016), measuring fluxes of $(6.47\pm\ 0.82)\times10^{-12}$ erg s^{-1}cm^{-2}deg^{-2} and $(2.90\pm\ 0.16)\times10^{-12}$ erg s^{-1}cm^{-2}deg^{-2} in the hard and soft bands, respectively. Excluding all sources with a hard band (2–10 keV) flux greater than 3×10^{-15} erg s^{-1}cm^{-2}deg^{-2} from the mock catalogue (we assume that above this threshold the data from Civano et al. 2016 is nearly complete), the remaining fluxes are 10.02×10^{-12} and 3.46×10^{-12} erg s^{-1}cm^{-2}deg^{-2}, which differ by 55 per cent (2.75σ) and 19 per cent ($\sim 1\sigma$),[7] in the hard and soft bands, respectively.

This indicates that the flux of faint sources in the mock catalogue is in slight tension with the CXB, in the hard band.[8] In the right panel of Fig. 5, the number counts are partitioned into CTK and CTN number counts. Although the CTN number counts agree well with the observations, the inclusion of the CTK AGN leads to an overestimation. This suggests that ILLUSTRISTNG overestimates the intermediate-luminosity AGN population ($\log(L_X)$=42–44 erg s^{-1}), a conclusion that aligns with the findings of previous studies (Weinberger et al. 2018; Habouzit et al. 2019, 2021).

Conversely, the issue could be in the modelling of the X-ray properties. It has been suggested that some AGN might be intrinsically X-ray weak (Pu et al. 2020), and this fraction might be significant for some populations (e.g. high Eddington ratio AGN; Laurenti et al. 2022, see also Nardini et al. 2019). As discussed in the previous section, the mock catalogue accounts for this effect by assuming a distribution on the bolometric corrections, and the fraction of X-ray weak,[9] sources is 12.5 per cent. Consequently, assuming that ILLUSTRISTNG provides an accurate representation of the universe, to comply with the CXB, both a very high CTK fraction and intrinsic X-ray weakness (with a fraction greater than 12.5 per cent) are required among the general AGN population.

The right panel of Fig. 5 also illustrates the number counts, assuming a radiative efficiency of $\epsilon_r = 0.2$ in the luminosity model (cyan line), the fiducial value assumed by ILLUSTRISTNG. These number counts significantly exceed observational constraints, across the full flux range, indicating that a lower value is necessary to match the observed values. As Sijacki et al. (2015) point out for the original ILLUSTRIS, in these models, the radiative efficiency is degenerate with the SMBH feedback efficiency, therefore, ILLUSTRISTNG cannot uniquely constrain this parameter. For this reason, a value of $\epsilon_r = 0.08$ was adopted, to ensure a reasonable match to the number counts. Fig. 5 also presents the number counts based on the luminosity model by Weinberger et al. (2018, magenta line), assuming $\epsilon_r = 0.08$. These number counts also significantly exceed observational constraints, further illustrating the impact of the numerical prefactor in the low Eddington ratio branch of the model.

It is worth highlighting that while we assume a constant radiative efficiency and a constant prefactor on the ADAF, both of these quantities depend on the spin of the SMBH (Griffin et al. 2019; see also the discussion in Amarantidis et al. 2019), which is not tracked by ILLUSTRISTNG. Considering the impact of these parameters on the number counts, it would be worthwhile to include subgrid modelling of the SMBH spin in future large-scale cosmological simulations. An example of subgrid spin modelling was already adapted to ILLUSTRISTNG (in a small cosmological volume), as presented by Bustamante & Springel (2019), and has shown success in mitigating some of the discrepancies observed in the fiducial run.

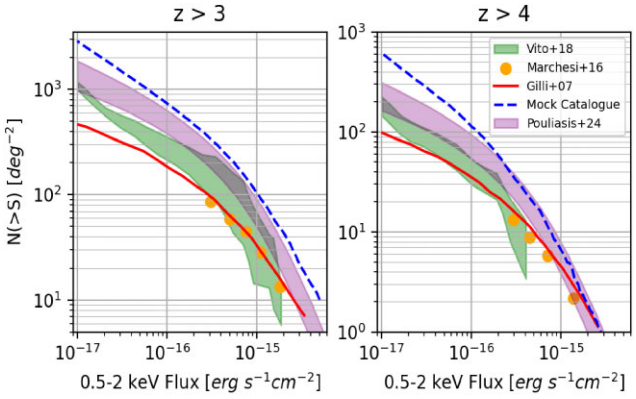

Figure 6. Comparison of cumulative high-redshift AGN number counts in the 0.5–2 keV flux band from the mock catalogue with observations. The left panel shows counts for $z > 3$, and the right for $z > 4$. Observational data are represented by the green-shaded region (Vito et al. 2018) and orange points (Marchesi et al. 2016). Predictions from the mock catalogue (blue line, Gilli et al. 2007) CXB model (red line) and the (Pouliasis et al. 2024) XLF (purple band) are also shown.

2.5 Comparison with high-redshift observations

We also plot the cumulative number counts at high-z in Fig. 6, for $z > 3$ (left plot) and $z > 4$ (right plot), comparing with observations from Marchesi et al. (2016), Vito et al. (2018), as well as the Gilli et al. (2007) CXB model. Although these observations are consistent for higher fluxes, discrepancies arise at fainter flux levels, below 10^{-16} erg s^{-1}cm^{-2}, highlighting the current uncertainty surrounding the high-redshift AGN population. The mock catalogue exhibits a ∼threefold excess of AGN at the faintest fluxes, highlighting a divergence with these observations.

The recent work by Pouliasis et al. (2024) studied the high-redshift XLF and found a higher space density of AGN at $z > 3$, compared to Gilli et al. (2007), Marchesi et al. (2016), and Vito et al. (2018), most significantly for $L_X > 10^{44}$ erg s^{-1}. The number counts predicted

[7] Assuming, again, that the uncertainty in this measurement is 20 per cent.
[8] If a lower threshold of 2×10^{-15} erg s^{-1}cm^{-2}deg^{-2} is adopted, the unresolved fluxes are 8.55×10^{-12} and 2.77×10^{-12} erg s^{-1}cm^{-2}deg^{-2} in the hard and soft bands, respectively, therefore, while the flux values are highly sensitive to the chosen threshold, the excess of flux in the hard band remains evident.
[9] X-ray weak by a factor of 10, relative to the relation from Duras et al. (2020).

from the integration of this XLF are also shown in the figure, with 1σ uncertainties obtained from 10 000 Monte Carlo realizations that propagate the parameter uncertainties reported for the PDE fit in table 2 of Pouliasis et al. (2024).[10] These number counts show much better agreement with the mock catalogue, suggesting that the discrepancy between the mock catalogue and Vito et al. (2018) could be attributed to the limited number of bright AGN within the small survey area of CDFS. However, while this may explain the deviation at higher fluxes, it does not account for the discrepancy at the faintest fluxes.

Over the past two years, *JWST* has identified a significantly larger number of AGN candidates at high redshift, compared to previous observations. The recent work by Lyu et al. (2024) presents a high-redshift sample with 20 *JWST*-selected AGN (candidates) and 2 pre-*JWST*-selected AGN, at $z > 4$. If confirmed, this implies a tenfold increase in AGN detections, and with a survey area of 34 arcmin^2, this would correspond to 2330 AGN[11] deg^{-2}.

The higher number of AGN (candidates) identified by *JWST* suggests that current X-ray surveys could be missing a substantial fraction of the high-redshift AGN population. The disparity between the predictions from the mock catalogue and the X-ray observations, at the faintest fluxes, may result from the limitations of current X-ray telescopes, which struggle to detect AGN at high redshifts.

Recent *JWST* observations also find a higher black hole accretion rate density (i.e. the average accretion rate, per comoving volume element, which quantifies the average growth of the AGN population), by a factor of $\sim$3, more consistent with the predictions from cosmological simulations (Yang et al. 2023; Pouliasis et al. 2024). Considering this, even though the predictions from the mock catalogue might be too optimistic, they offer valuable insight into an unexplored AGN population that recent *JWST* observations are beginning to unveil.

This comparison emphasizes the value of cosmological simulations of galaxy formation to assess the true abundance and properties of AGN, as well as to make predictions for future observatories (see also Habouzit 2024 for a recent comparison of cosmological simulations with results from *JWST*). Considering all of this, the mock catalogue appears to be robust to simulate the NewAthena survey.

3 WFI SURVEY SIMULATION

3.1 SIXTE

In this work, we adopt the SIXTE software, a mission-independent Monte Carlo simulation package for X-ray observatories (Dauser et al. 2019). SIXTE was installed on Sciserver,[12] a collaborative research platform that provides access to large scientific data sets, computational tools, and cloud-based resources, allowing researchers to analyse and share data efficiently.

SIXTE operates in a fully modular approach, comprising three fundamental steps: photon generation, photon imaging, and event detection. The input source catalogue follows the conventions of the SIMPUT format (Schmid, Smith & Wilms 2013), and is used to generate an initial photon list. This list contains the arrival time, energy, and position of each photon, which are determined through a Monte Carlo process based on the instrument's effective area, FOV, and attitude. This photon list is then convolved with the PSF and vignetting functions to generate an impact list of photons that reach the detector plane. Finally, this impact list is sent to the detector model, which simulates the event generation and readout process. The outcome of this process is a standardized event file that contains the read-out times, reconstructed energies, and detected positions of the photons. For further details, the reader is referred to Dauser et al. (2019).

3.2 Simulation process

We assume that the WFI will be used in a wide survey comprising 100 pointings (~ 44 deg^2). Of these, 70 pointings will have an exposure time of 200 ks, while the remaining 30 will have a deeper exposure of 300 ks.

Due to the time-consuming nature of these simulations, only nine pointings are simulated: 6 with 200 ks of exposure and 3 with 300 ks of exposure. The results are then scaled to represent the complete survey by multiplying the number of detections by $\frac{70}{6}$ for 200 ks and $\frac{30}{3}$ for 300 ks observations. These pointings are non-contiguous and chosen to ensure maximum separation across different areas of the light-cone, thus mitigating the impact of cosmic variance on our results. Oogi et al. (2023) use a large volume simulation, to present an in-depth discussion of the effect of cosmic variance in AGN surveys, finding that for an area of 10 deg^2, the cosmic variance is < 10 per cent, even at $z \sim 8$, for most of the AGN population, thus it should not significantly affect our results, except for the brightest sources (but see Section 5 for more on this).

The input catalogues include three types of source: AGN, non-active galaxies, and extended sources. Since this work focuses on AGN, and other sources are treated as background contamination, using cosmological simulations to generate additional catalogues for them was deemed unnecessary. Therefore, the mock catalogues developed by Marchesi et al. (2020) were utilized for the non-active galaxies and extended sources. Although these mock catalogues account for nearly all of the CXB, we must still include the diffuse galactic foreground from the local hot bubble and diffuse galactic emission. This foreground was added as an additional SIXTE file, adopting the model presented in appendix C of Zhang et al. (2020). The instrumental background is assumed to be flat over the FoV and is directly implemented within SIXTE, using the most up-to-date files for NewAthena. The WFI instrument comprises four physically separated detectors, creating a cross-shaped pattern of insensitive regions in the resulting image. To mitigate these gaps and achieve a more uniform coverage, we assumed a dithering pattern following a Lissajous curve (Zhang et al. 2020) with an amplitude of 0.025 deg.

Fig. 7 shows an example of an RGB image, of a WFI pointing, illustrating a future observation with NewAthena, with 200 ks of observation. The image shows several point sources, corresponding to AGN or non-active galaxies, as well as extended sources, such as galaxy groups or clusters. AGN presents a variety of colours, due to different spectral properties.

3.3 Detection methodology

Source detection is performed in the soft band (0.5–2 keV), since this is the most sensitive band and ensures the best S/N for NewAthena, due to the lower effective area at higher energies. Furthermore, because of the varying exposures across different regions of the image (gaps and borders), each image is normalized by the corresponding exposure map before running the detection pipeline.

Source detection was performed using the Source Extractor software (SExtractor; Bertin & Arnouts 1996). SExtractor is a

[10]This does not take into account the correlations of the parameters, that are presented in fig. 7 of Pouliasis et al. (2024). If these correlations were included, the result would be a broadening of the uncertainty band.
[11]This estimate is also subject to considerable cosmic variance.
[12]https://www.sciserver.org/

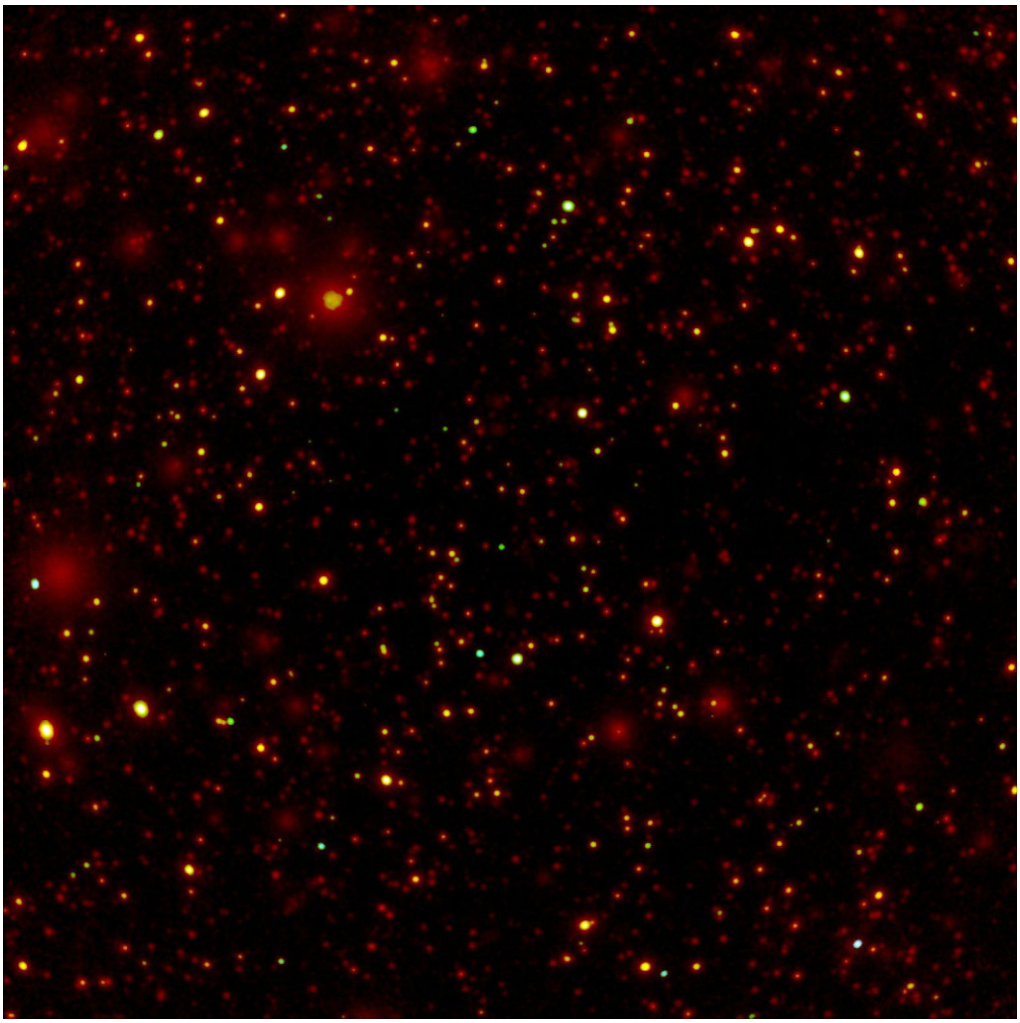

Figure 7. RGB colour image of a WFI FOV (40 arcmin × 40 arcmin), with 200 ks of observation time. The red band corresponds to 0.5–2 keV, the green band to 2–4.5 keV, and the blue band to 4.5–10 keV. The image is on a logarithmic scale and is smoothed.

versatile software package originally developed for source detection in optical images. However, it has been successfully used in X-ray images, provided that they are appropriately filtered (e.g. Valtchanov, Pierre & Gastaud 2001; Pacaud et al. 2006; Zhang et al. 2020). The initial filtering step is crucial to denoise the image, thus reducing the number of spurious detections found by SExtractor. There are many approaches to denoise an astronomical image (see Roscani et al. 2020 for a recent work comparing different denoising algorithms) and wavelet filtering is a very effective approach for X-rays.

The denoising process involves three steps: first, the image is subjected to a wavelet transform that decomposes it into various frequency components represented by wavelet coefficients. Second, thresholding is applied, reducing or setting to zero the smaller coefficients likely representing noise and retaining the larger coefficients that correspond to signal features. Lastly, an inverse wavelet transform is applied to reconstruct the data, yielding a denoised image, where noise is suppressed and essential features are preserved. This algorithm was implemented using the PYTHON routine: 'denoise_wavelet' from the scikit-image[13] library.

To calibrate the denoising algorithm, the framework developed by Batson & Royer (2019) was adopted. This approach focuses on minimizing the self-supervised loss,[14] which quantifies the average difference between filtered and noisy images. Under the assumption that the noise exhibits statistical independence, while the true signal exhibits some correlation, this metric enables an objective comparison between different filters, based solely on the noisy data. Using this criterion, all discrete wavelets[15] from the PyWavelets[16] library were tested. The best results were obtained with the wavelet coif1 of the coiflet family and 1 decomposition level.[17] After choosing this wavelet, the calibration process was repeated to select the best noise standard deviation, used to calculate the thresholds, for each image. Fig. 8, compares the unfiltered and filtered versions of a (zoomed) image, with 300 ks of observation. As shown in the figure, the noise is suppressed without significant blurring of the sources.

[13] https://scikit-image.org/

[14] It is called self-supervised since it does not require knowledge of the ground truth.

[15] Other algorithms available in the library, namely: the bilateral filter, non-local means, and total variance were also tested, however, none of these was successful.

[16] https://pywavelets.readthedocs.io/en/latest/

[17] Using more than one decomposition level reduces the positional accuracy of the detected sources.

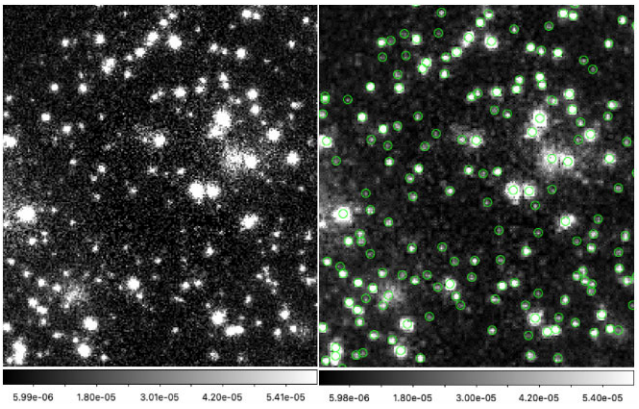

Figure 8. Comparison of unfiltered (left panel) and filtered (right panel) views of a simulated ATHENA/WFI zoomed FOV (9 arcmin × 9 arcmin, 300 ks exposure, and 0.5–2 keV soft band). The count rate is plotted in the colour bar. The green circles are the sources detected by SEXTRACTOR.

Following this pre-processing step, SEXTRACTOR was applied to each image. The objects were selected with a 3σ threshold, per pixel, on a minimum area of 3 contiguous pixels. These objects were deblended assuming 64 levels, with a minimum contrast of 0.005. The background map was also used as a weight map, to account for the different exposures, across different regions of the image. Photometry was performed using SEXTRACTOR's automatic aperture photometry, following Kron (1980) and Infante (1987). Although source detection was conducted on the filtered image, the photometry was extracted from the original image.

After extracting the sources, they are cross-matched with the input catalogues. This cross-match was performed using TOPCAT,[18] assuming a maximum separation of 5 arcmin and selecting as valid cross-matches those that were symmetric. We matched the output catalogue with the three input catalogues and in cases where the cross-match radius was compatible with both an AGN and a galaxy, the source with the highest flux was taken as the counterpart. Sources without match in the input catalogues are classified as spurious. A flux limit[19] of 5×10^{-17} erg s^{-1}cm^{-2} was applied to the input catalogues, to mitigate the possibility of coincidence matching of faint sources with spurious background fluctuations.

3.3.1 *Completeness and reliability*

With this pipeline, we measure, on average, a 4 per cent spurious source fraction in the survey. Specifically, this fraction is expected to be 4.4 per cent in pointings with 200 ks of exposure and 3.1 per cent with 300 ks of exposure. The image borders have a much lower exposure, contributing to a larger spurious fraction. If these are excluded, retaining 90 per cent of the central area, the average spurious fraction reduces to 3.0 per cent (3.2 per cent for 200 ks and 2.6 per cent for 300 ks, respectively).

Next, we consider the completeness of the survey, defined as the fraction of input sources successfully detected. This is plotted as a function of the input soft band flux, shown cumulatively in the left panel of Fig. 9 and differentially, in the right panel of the same figure. The fraction of detected sources is greater than 95 per cent for high fluxes, above 10^{-15} erg s^{-1}cm^{-2}, dropping to around

[18] https://www.star.bris.ac.uk/ mbt/topcat/

[19] This is the predicted (soft band) confusion limit for a 9 arcmin PSF.

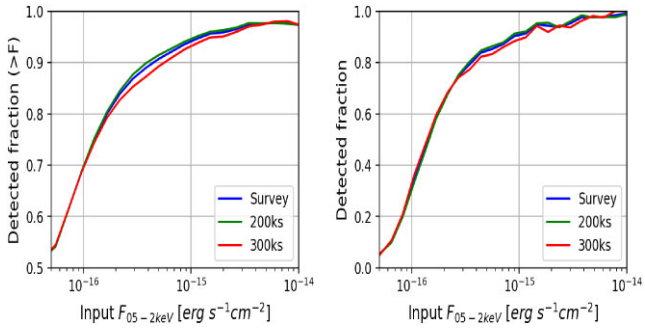

Figure 9. Left: cumulative completeness curves as a function of input flux ($F_{0.5-2keV}$) for different survey exposure times. The blue curve represents the baseline survey, while green and red correspond to 200 and 300 ks exposures. Right: the same as the left panel, but binned in flux.

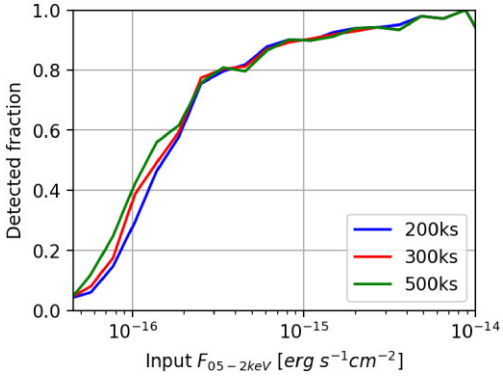

Figure 10. The plot compares the completeness as a function of input soft band flux (0.5–2 keV) for three different exposure times: 200 ks (blue line), 300 ks (red line), and 500 ks (green line), in the same FOV. Deeper exposures consistently show higher detection fractions, at lower flux values, reflecting the improved sensitivity of longer exposure times.

50 per cent, for fluxes above 5×10^{-17} erg s^{-1}cm^{-2}. The 80 per cent completeness flux limit for this survey is 3.8×10^{-16} erg s^{-1}cm^{-2}, while the 20 per cent completeness flux limit is 8.8×10^{-17} erg s^{-1}cm^{-2}. The figure also shows the completeness in the pointings with 200 ks (green line) and 300 ks (red line) of exposure. Visual inspection of undetected sources indicates that the primary cause of incompleteness, at high flux levels (i.e. above 10^{-15} erg s^{-1}cm^{-2}), is source blending, predominantly with other AGN. None the less, extended sources also contribute significantly to the incompleteness at fainter fluxes. This is evident in the 300 ks completeness curve, which falls below the 200 ks curve within the flux range of 2×10^{-16} to 2×10^{-15} erg s^{-1} cm^{-2}. The reduction in completeness in the deeper exposure is primarily due to the presence of two bright clusters within one of the simulated pointings.

Surprisingly, the completeness seems to be independent of the exposure of the survey. This is unexpected since increasing the exposure time increases the S/N, thus it should improve the completeness for faint sources. To further investigate this, Fig. 10 plots the completeness curves for the same FOV, with 200 ks of exposure (blue line), 300 ks of exposure (red line), and 500 ks of exposure (green line). The figure demonstrates that deeper observations achieve better completeness for faint fluxes. The absence of this trend in the previous figure is probably due to the cosmic variance among different pointings of the WFI. The completeness curves converge

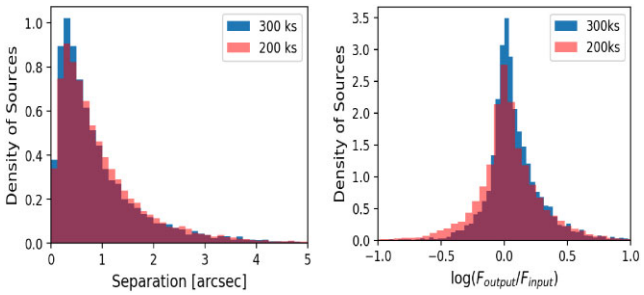

Figure 11. Left panel: histogram of AGN separations between input and detected positions, in arcseconds, comparing data with 200 ks (red) and 300 ks (blue) exposures. The distributions show the normalized frequency of separations between detected sources. Right panel: histogram of the normalized source fraction versus the logarithmic flux ratio, $\log(F_{\rm output}/F_{\rm input})$, for 200 ks (blue) and 300 ks (red) exposures. The distribution is centred around zero, indicating accurate flux recovery, with the 300 ks exposure reducing the negative tail, suggesting a more accurate flux recovery for longer exposures.

at 5×10^{-17} erg s^{-1}cm^{-2}, which indicates that below this flux, the survey is confused and deeper exposures will not improve the depth.

3.3.2 Astrometric and photometric accuracy

Another important factor to evaluate is the positional accuracy of the AGN, which is crucial to ensure that multiwavelength counterparts can be found. The left panel of Fig. 11 plots the difference between the input and detected positions of AGN observed with 200 ks (red histogram) or 300 ks (blue histogram). The median separation of detected AGN is 0.64 arcmin for the 300 ks exposure and 0.71 arcmin for the 200 ks exposure. Additionally, the fraction of AGN with separations less than 1 arcmin is 68 per cent for 300 ks and 65 per cent for 200 ks.

Finally, we assess the accuracy of the detected fluxes. To calibrate the measurements, we use bright AGN with fluxes above 10^{-14} erg s^{-1}cm^{-2}, deriving a mean energy conversion factor of 2.5×10^{-13} erg cm^{-2}counts^{-1}. The right panel of Fig. 11 presents the ratio of detected to input flux for sources with $\log(N_{\rm H}) \leq 22$, comparing observations with 200 ks (blue histogram) and 300 ks (red histogram). While the flux ratios are centred around unity, they exhibit significant scatter. The 300 ks exposure results in a narrower negative tail, suggesting that deeper observations mitigate flux underestimation. Quantitatively, 69 per cent of AGN in 300 ks exposures have detected fluxes within 50 per cent of their true values, compared to 62 per cent for 200 ks. Additionally, 77 per cent of AGN exhibit flux ratios below 1.5, independently of exposure time. These findings suggest that flux underestimation primarily arises from the low photon counts of faint AGN, whereas overestimation is likely driven by contamination from nearby sources.

4 RESULTS

Each pointing of the WFI will detect ∼2800 point sources, on average, with 90.7 per cent identified as AGN and the remaining 9.3 per cent as non-active galaxies. The complete survey will find a total of ∼250 000 AGN, including ∼9000 CTK AGN. The predictions for this survey are presented in Table 1, while the detected sources are plotted in Fig. 13.

As shown in Table 1, NewAthena is expected to detect ∼21 000 AGN at $z > 3$ and ∼3200 AGN at $z > 4$. This is unprecedented among X-ray surveys, as the largest high-redshift sample, compiled by Pouliasis et al. (2024), includes ∼630 $z > 3$ and ∼100 $z > 4$ AGN, implying an improvement by a factor of ∼30. NewAthena will also enable the detection of a population of X-ray-selected AGN within the epoch of reionization (EoR), at $z > 6$. Currently, most of $z > 6$ AGN observed in the X-ray were pre-selected in the optical or near-IR (Wang et al. 2021) and blind X-ray detection is necessary to statistically constrain the properties of the AGN population (Pouliasis et al. 2024).[20] Recently, a few X-ray-selected AGNs were found at $z > 6$, (Wolf et al. 2021, 2023; Barlow-Hall et al. 2023), however, this is only possible for the most luminous sources ($L_{2-10\,\rm keV} > 10^{45}$ erg s^{-1}), and current facilities are unable to detect the bulk of the AGN population. NewAthena is expected to uncover X-ray sources two orders of magnitude fainter.

The source density derived by Marchesi et al. (2020) sets a good comparison point for our estimates since they were derived for the original ATHENA configuration and are purely based on observational constraints (XLF+CXB). Marchesi et al. (2020) predict 8220 AGN with $z > 3$, 1695 for $z > 4$, 385 for $z > 5$, 75 AGN for $z > 6$, and 21 for $z > 7$.[21] Our predictions diverge significantly for AGN at redshifts $z > 3$ and > 4, where our results are higher by factors of 2.6 and 1.8, respectively. Although there is a reasonable agreement for AGN at $z > 5$, our predictions are lower by factors of 2.4 at $z > 6$ and 1.9 at $z > 7$, in the EoR. Furthermore, considering the predictions for the CTK population, Marchesi et al. (2020) estimate 6700 AGN, with 219 at $z > 3$. In contrast, our predictions for CTK AGN at $z > 3$ are higher by a factor of 7. This is further discussed in Section 5.

Fig. 12 compares the $N_{\rm H}$ distribution of detected and input AGN. The figure demonstrates that NewAthena will be capable of detecting highly obscured AGN, including those with $N_{\rm H} > 10^{25}$ cm^{-2}, however, a strong selection bias remains against the most obscured AGN.

One advantage of creating catalogues with HDS is that these simulations track some intrinsic characteristics of the AGN, such as the SMBH mass or accretion rate. Fig. 13 illustrates the normalized distributions of SMBH masses, Eddington ratios (λ), hard X-ray luminosities, and photon indices (Γ) of the (detected) high-redshift AGN ($z > 3$), as well as the input AGN.[22] The figure shows that, according to ILLUSTRISTNG, most of the high-redshift AGN will be powerful quasars, with masses $\sim 10^8\,{\rm M}_\odot$, accreting very close to the Eddington limit, with a typical luminosity of $\sim 10^{44}$ erg s^{-1}. In addition, NewAthena might be able to uncover some AGN with SMBH masses as low as $\sim 5 \times 10^6\,{\rm M}_\odot$. When comparing the input and detected populations, it becomes evident that low-mass SMBHs power the majority of high-redshift AGN and highlights that the observed sample is not representative of the input population. The distribution of Eddington ratios spans a wide range, with the majority of SMBHs accreting at a small fraction of the Eddington limit, typically a few percent, consistent with an ADAF scenario. Nevertheless, AGNs accreting near the Eddington limit constitute a considerable fraction of the input population, indicating a diverse range of accretion states. The photon indices present a similar distribution, indicating that there is no bias in this quantity.

[20] If pre-selection is used, the survey's selection function becomes unclear, leading to potential biases in the conclusions drawn.
[21] These numbers are rescaled to 100 WFI pointings, since Marchesi et al. (2020) assumed 108 WFI pointings in their Mock Observing Plan.
[22] No flux limit is assumed in the input distribution.

Table 1. Predictions for the survey of the NewAthena mission. These results are extrapolated from nine pointings taken from a grid in the mock catalogue. The different columns show a breakdown of the number of detected AGN above a given redshift threshold, as well as the logarithm of the 0.5–2 keV luminosity, assuming a flux of 5×10^{-17} erg s^{-1}cm^{-2}. The first row presents the results for all sources, while the second row only considers CTK AGN.

	$z>1$		$z>2$		$z>3$		$z>4$		$z>5$		$z>6$		$z>7$	
	$N_{\rm src}$	$L_{\rm lim}$	$N_{\rm src}$	$L_{\rm lim}$	$N_{\rm src}$	$L_{\rm lim}$	$N_{\rm src}$	$L_{\rm lim}$	$N_{\rm src}$	$L_{\rm lim}$	$N_{\rm src}$	$L_{\rm lim}$	$N_{\rm src}$	$L_{\rm lim}$
All AGN	187 505	41.4	86 237	42.2	21 046	42.6	3190	42.8	435	43.0	35	43.2	11	43.4
CTK AGN	7442	43.3	5335	43.7	1601	44.0	193	44.2	11	44.3	0	–	0	–

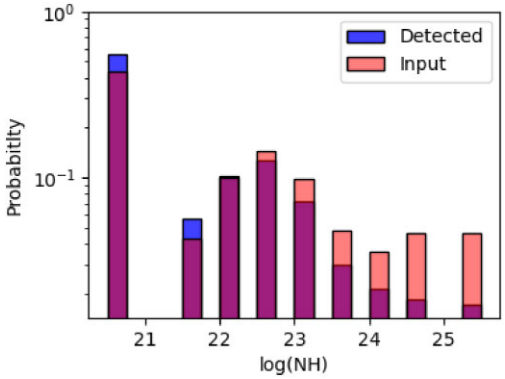

Figure 12. Distribution of column density for input (red) and detected (blue) AGN. The input AGN have a flux limit of 5×10^{-17} erg s^{-1}cm^{-2}.

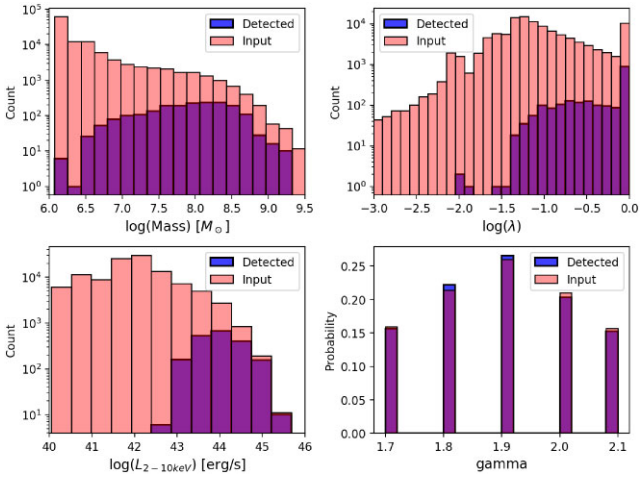

Figure 13. Comparison of input and detected AGN at $z > 3$. The histograms show the distributions of SMBH mass (upper left panel), Eddington ratio (λ) (upper right panel), X-ray luminosity ($L_{\rm X}$) (lower left panel), and photon index (Γ) (lower right panel) for both input (red) and detected (blue) populations. Detected sources tend to have higher masses, X-ray luminosities, and Eddington ratios, with similar distributions for Γ.

5 DISCUSSION

As stated in Marchesi et al. (2020), one of the goals for the Mock Observing Plan of the original ATHENA was to detect at least 10 AGN at $7 < z < 8$ with $44 < \log(L_{0.5-2\,\rm keV}) < 44.5$. According to our predictions, NewAthena will also achieve this goal. No AGN at $z > 6$ with $\log(L_{0.5-2\,\rm keV}) < 43.5$ was detected in the simulated survey area (9 per cent of the total), despite the input catalogue containing 8 of these AGN. This suggests that significantly deeper exposures would be necessary to detect such sources.

Since NewAthena is a rescoped version of ATHENA, it is insightful to compare our predictions with the predictions for the original wide survey. As discussed in the previous section, the predictions for AGN in the redshift range $3 < z < 5$ are higher by a factor of ∼2. This increase can be attributed to the higher number of high-redshift AGN in the mock catalogue, as illustrated by Fig. 6, compared to the mocks used by Marchesi et al. (2020).

Notably, the predictions for the EoR are approximately half of what is predicted by Marchesi et al. (2020). This discrepancy is probably due to the higher levels of obscuration assumed in our mock. While Marchesi et al. (2020) adopt a constant CTK fraction of $\frac{4}{9}$, the mock catalogue employs a redshift-and-luminosity-dependent CTK fraction. In addition, ISM obscuration is taken into account, assuming the model of Gilli et al. (2022), in which the median column density of the host galaxy becomes CTK at $z > 6$.

Finally, it is necessary to acknowledge that HDS face substantial difficulties in reproducing the most luminous AGN ($L_X > 10^{45}$ erg s^{-1}) observed at high redshift, possibly due to limitations in volume and resolution (Weinberger et al. 2018; Amarantidis et al. 2019). Specifically, ILLUSTRISTNG is unable to simulate SMBHs more massive than 5×10^7 M$_\odot$ at $z > 6$, and assumes Eddington limited accretion, which restricts the maximum attainable luminosity. For this reason, the number of detected EoR AGN could be higher than these predictions.

Nevertheless, these findings are encouraging, as they demonstrate NewAthena's capability to detect a population of X-ray-selected AGN during the EoR, even with the revised mission specifications and higher levels of obscuration.

5.1 CTK AGN detection

Regarding the detection of CTK AGN, the total number of these sources significantly exceeds the predictions by Marchesi et al. (2020), with a discrepancy by a factor of 7 at $z > 3$.[23] This increase can be attributed to a higher overall number of AGN in the mock catalogue and the assumption of a CTK fraction that increases with redshift. This aligns well with the most recent results from *JWST*, which suggest a greater prevalence of CTK AGN at high redshifts (Lyu et al. 2024; Maiolino et al. 2024), however, large uncertainties remain since *JWST* is unable to directly constrain the column densities and X-ray luminosities of these X-ray weak AGN.

If our predictions hold, NewAthena will detect a significant number of CTK AGN until $z \sim 4$ and may even detect a few sources at $z > 5$. This would represent a key advancement in understanding these rare, highly obscured sources at high redshifts. Detecting CTK AGN at such early times could provide essential clues about the formation and growth of SMBH, as well as the role of these objects in the evolution of galaxies. This is discussed further in Section 5.3.

[23]By definition, only AGN with $N_{\rm H} \geq 1.5 \times 10^{24}$ cm^{-2} are classified as CTK, so only AGN with $log(N_{\rm H}) \geq 24.18$ are considered CTK.

5.2 Comparison with theoretical estimates

Our predictions are 2 dex lower than those presented in Habouzit et al. (2021) with ILLUSTRISTNG, across all redshifts. This discrepancy is attributed to differences in the modelling of X-ray properties, including the bolometric luminosity model, radiative efficiency, and bolometric corrections, as well as the higher obscuration assumed in this study. Additionally, realistic Monte Carlo simulations were conducted, accounting for background and foreground contaminants, and the AGNs were detected using a source detection pipeline, instead of applying a simple luminosity limit.

This significant discrepancy highlights the critical role that post-processing assumptions play in the creation of mock catalogues and predictions for future missions. As discussed in Section 2.4, accurate modelling of the X-ray properties, down to the faintest AGN, is essential to align the predictions of cosmological simulations with observational constraints, such as the CXB, and ensure robust estimates.

5.3 Survey observing strategy and limitations

Comparing the survey performance between pointings with 200 and 300 ks of exposure reveals minimal gains in completeness, as shown in Fig. 9, with the 300 ks pointings detecting only an average of 100 additional AGN. However, a deeper exposure increases the number of counts per source, resulting in more accurate estimates of properties such as flux, as demonstrated in Fig. 11. Importantly, all detected AGN at $z > 6$ were found in 200 ks exposures, suggesting that this is sufficient to reach the EoR, until $z\sim 8$. Given the significant time investment required for the deeper exposures (3 Ms), a rigorous evaluation of whether the increase in S/N improves the overall scientific return of the survey is essential.

The main limitation of this work is the reliance on a single cosmological simulation: ILLUSTRISTNG. As discussed in Amarantidis et al. (2019) and Habouzit et al. (2021), different simulations employ distinct subgrid modelling, which substantially affects the evolution and properties of SMBH, thus producing different AGN populations. Consequently, the results presented here may not be fully representative of the theoretical understanding of AGN.

This limitation can be addressed in future work, comparing the results of mock catalogues from different cosmological simulations, with several promising candidates among the state-of-the-art HDS. For instance, the MILLENNIUMTNG simulation (Kannan et al. 2023; Pakmor et al. 2023); the FLAMINGO simulation (Schaye et al. 2023); the ASTRID simulation (Ni et al. 2022, 2024), or the SIMBA simulation (Davé et al. 2019).

An additional limitation concerns the source detection and extraction methodology. Although the current methodology ensures high completeness, reliability, and astrometric accuracy, it fails to accurately extract counts from sources, especially if they are blended or contaminated.

An important improvement to the source detection pipeline would be to implement model-fitting capabilities, incorporating the PSF and extended source models. Such an improvement would not only increase the photometric accuracy by optimizing the S/N but would also enable more accurate measurements of blended or contaminated sources. Furthermore, this approach would enable the calculation of detection likelihoods, ultimately improving the reliability of source detections.

Future work could address this by adapting existing software, such as the *emldetect* from the XMM-SAS package[24] or explore alternative approaches (e.g. machine learning; Xu & Zhu 2024).

Finally, while our predictions suggest the detection of a significant number of CTK AGN, we have not evaluated whether their column density can be accurately constrained, which is crucial for their proper characterization. Future work should perform spectral analysis of the detected AGN to address this limitation and assess NewAthena's ability to distinguish between intrinsically X-ray weak and CTK AGN. Additionally, it is important to investigate the impact of exposure time on X-ray spectra, as observations with 500 ks remain feasible despite the effects of source confusion.

6 SUMMARY AND CONCLUSIONS

This work focused on simulating NewAthena's capabilities to detect faint AGN. Using the ILLUSTRISTNG cosmological simulation, a comprehensive mock catalogue of X-ray AGN was created and processed through an end-to-end simulation framework, with the SIXTE software. The analysis explored key aspects such as the completeness, reliability, and sensitivity of the survey, with a particular emphasis on the detection of high-redshift and CTK AGN. The results demonstrated that NewAthena will significantly improve the detection of faint AGN populations, compared to current surveys, providing the first statistically significant X-ray-selected sample of AGN in the EoR and advancing our understanding of AGN evolution in the early universe.

Our main findings can be summarized as:

(i) A state-of-the-art hydrodynamical cosmological simulation, ILLUSTRISTNG, was used to create the X-ray AGN mock catalogue that spans 10 deg^2 and covers the redshift range 0–12. This involved the construction of a light-cone from the discrete snapshots and applying corrections to account for the limited resolution of the simulation. These corrections have a significant impact on high-redshift predictions.

(ii) We determined the X-ray properties of the SMBH in post-processing, assuming a bolometric luminosity model, X-ray bolometric corrections, an obscuration model and realistic spectral templates. We also demonstrate that the radiative efficiency and the low Eddington ratio AGN have a significant impact on the number counts, emphasizing the necessity to integrate subgrid prescriptions to track the SMBH spin in future large-scale cosmological simulations.

(iii) During the validation process, we noticed an overabundance of faint AGN. However, this discrepancy can be alleviated by the assumption of a high CTK fraction and intrinsic X-ray weakness, suggested by recent *JWST* observations.

(iv) We simulate the NewAthena survey and prove that it will significantly improve the statistics of high-redshift AGN ($z > 3$), and uncover a population of X-ray-selected AGN in the EoR. Nevertheless, only AGN with luminosities exceeding $10^{43.5}$ erg s^{-1} are expected at these redshifts. Our results also suggest a higher number of CTK AGN than previously predicted, even beyond $z > 4$.

(v) The analysis of WFI pointings with varying exposure times indicates that deeper observations with 500 ks remain feasible, despite the challenges posed by source confusion.

In summary, this work contributes to our understanding of high-redshift AGN populations, emphasizing the implications for the NewAthena mission.

[24] https://www.cosmos.esa.int/web/xmm-newton/sas

ACKNOWLEDGEMENTS

We thank the referee for the helpful comments and ideas that improved this manuscript. NC, IM, and JA acknowledge financial support from the Science and Technology Foundation (FCT, Portugal) through research grants UIDB/04434/2020 (doi:10.54499/UIDB/04434/2020) and UIDP/04434/2020 (doi:10.54499/UIDP/04434/2020). GL, SM, and AC acknowledge financial support from the European Union's Horizon 2020 Programme under the AHEAD2020 project (grant agreement no. 871158) and the 'Accordo Attuativo ASI-INAF' no. 2019-27-HH.0. PP was supported by FCT Principal Investigator contract CIAAUP-092023-CTTI.

DATA AVAILABILITY

ILLUSTRISTNG data are available at: https://www.tng-project.org/

REFERENCES

Aird J., Coil A. L., Georgakakis A., Nandra K., Barro G., Pérez-González P. G., 2015, MNRAS, 451, 1892
Akylas A., Georgantopoulos I., 2021, A&A, 655, A60
Amarantidis S. et al., 2019, MNRAS, 485, 2694
Amarantidis S., 2021, Doctoral thesis, https://repositorio.ul.pt/handle/10451/50405
Ananna T. T., et al., 2019, ApJ, 871, 240
Ananna T. T., et al., 2022, ApJ, 939, L13
Antonelli V. et al., 2024, in Space Telescopes and Instrumentation 2024: Ultraviolet to Gamma Ray, p. 1272
Arnaud K., 1996, in Jacoby G. H., Barnes J., eds., ASP Conf. Ser. 101, Astronomical Data Analysis Software and Systems V, p. 17
Barlow-Hall C. L., Delaney J., Aird J., Evans P. A., Osborne J. P., Watson M. G., 2023, MNRAS, 519, 6055
Barret D. et al., 2018, in Space Telescopes and Instrumentation 2018: Ultraviolet to Gamma Ray, SPIE, p. 324. https://www.spiedigitallibrary.org/conference-proceedings-of-spie/10699/106991G/The-ATHENA-X-ray-Integral-Field-Unit-X-IFU/10.1117/12.2312409.full
Barret D. et al., 2023, Exp. Astron., 55, 373
Barrière N. M., Bavdaz M., Collon M. J., Ferreira I., Girou D., Landgraf B., Vacanti G., 2022, Handbook of X-ray and Gamma-ray Astrophysics, Springer Nature, Singapore, p. 1. http://arxiv.org/abs/2206.11291
Batson J., Royer L., 2019, in Proceedings of the 36th International Conference on Machine Learning, PMLR, p. 524, https://proceedings.mlr.press/v97/batson19a.html
Bertin E., Arnouts S., 1996, A&AS, 117, 393
Biffi V., Dolag K., Merloni A., 2018, MNRAS, 481, 2213
Brandt W. N., Alexander D. M., 2015, A&AR, 23, 1
Buchner J. et al., 2015, ApJ, 802, 89
Buchner J., Bauer F. E., 2017, MNRAS, 465, 4348
Buchner J., Schulze S., Bauer F. E., 2017, MNRAS, 464, 4545
Bustamante S., Springel V., 2019, MNRAS, 490, 4133
Cappelluti N. et al., 2017, ApJ, 837, 19
Carroll C. M., Ananna T. T., Hickox R. C., Masini A., Assef R. J., Stern D., Chen C.-T. J., Lanz L., 2023, ApJ, 950, 127
Churazov E., Sazonov S., Sunyaev R., Forman W., Jones C., Boehringer H., 2005, MNRAS, 363, L91
Circosta C. et al., 2019, A&A, 623, A172
Civano F. et al., 2016, ApJ, 819, 62
Collon M. J. et al., 2017, in Pareschi G., O'Dell S. L.eds, Optics for EUV, X-Ray, and Gamma-Ray Astronomy VIII. SPIE, San Diego, USA, p. 11, https://www.spiedigitallibrary.org/conference-proceedings-of-spie/10399/2273704/Development-of-Athena-mirror-modules/10.1117/12.2273704.full
Comparat J. et al., 2019, MNRAS, 487, 2005
Cruise M. et al., 2024, Nat. Astron, 9, 36
D'Amato Q. et al., 2020, A&A, 636, A37
D'Onofrio M., Marziani P., Chiosi C., 2021, Front. Astron. Space Sci., 8
Dauser T. et al., 2019, A&A, 630, A66
Davé R., Anglés-Alcázar D., Narayanan D., Li Q., Rafieferantsoa M. H., Appleby S., 2019, MNRAS, 486, 2827
Di Matteo T., Angles-Alcazar D., Shankar F., 2023, Massive Black Holes in Galactic Nuclei: Theory and Simulations, preprint, http://arxiv.org/abs/2304.11541
Done C., 2010, Observational Characteristics of Accretion onto Black Holes, preprint, http://arxiv.org/abs/1008.2287
Duras F. et al., 2020, A&A, 636, A73
Edgar R. G., 2004, New Astron. Rev., 48, 843
Fabian A. C., 2012, ARA&A, 50, 455
Georgantopoulos I., Akylas A., 2019, A&A, 621, A28
Gilli R. et al., 2022, A&A, 666, A17
Gilli R., Comastri A., Hasinger G., 2007, A&A, 463, 79
Gordon C., Arnaud K., 2021, Astrophysics Source Code Library, record ascl:2101.014
Griffin A. J., Lacey C. G., Gonzalez-Perez V., Lagos C. D. P., Baugh C. M., Fanidakis N., 2019, MNRAS, 487, 198
Gupta K. K. et al., 2021, MNRAS, 504, 428
Habouzit M. et al., 2019, MNRAS, 484, 4413
Habouzit M. et al., 2021, MNRAS, 509, 3015
Habouzit M. 2024, Is the James Webb Space Telescope Detecting Too Many AGN Candidates?, preprint, http://arxiv.org/abs/2405.05319
Hickox R. C., Alexander D. M., 2018, ARA&A, 56, 625
Hirschmann M., Dolag K., Saro A., Bachmann L., Borgani S., Burkert A., 2014, MNRAS, 442, 2304
Infante L., 1987, A Faint Object Processing Software: Description and Testing, Vol. 183, p. 177
Jovanović P., Popović L., 2009, X-ray Emission From Accretion Disks of AGN: Signatures of Supermassive Black Holes, preprint, http://arxiv.org/abs/0903.0978
Jun H. D., Assef R. J., Carroll C. M., Hickox R. C., Kim Y., Lee J., Ricci C., Stern D., 2021, ApJ, 906, 21
Kannan R. et al., 2023, MNRAS, 524, 2594
Kormendy J., Ho L. C., 2013, ARA&A, 51, 511
Kormendy J., Richstone D., 1995, ARA&A, 33, 581
Koulouridis E. et al., 2018, A&A, 620, A4
Kron R. G., 1980, ApJS, 43, 305
Laloux B. et al., 2022, MNRAS, 518, 2546
Lambrides E. L., Chiaberge M., Heckman T., Gilli R., Vito F., Norman C., 2020, ApJ, 897, 160
Lanzuisi G. et al., 2018, MNRAS, 480, 2578
Laurenti M. et al., 2022, A&A, 657, A57
Liu T. et al., 2017, ApJS, 232, 8
Liu B. F., Taam R. E., 2013, ApJS, 207, 17
Luo B. et al., 2016, ApJS, 228, 2
Lyu J. et al., 2024, ApJ, 966, 229
Mahadevan R., 1997, ApJ, 477, 585
Maiolino R. et al., 2024, MNRAS, 538, 1921
Marchesi S. et al., 2016, ApJ, 827, 150
Marchesi S. et al., 2020, A&A, 642, A184
Marinacci F. et al., 2018, MNRAS, 580, 5113
Masini A. et al., 2020, ApJS, 251, 2
Morganti R., 2017, Front. Astron. Space Sci., 4
Naiman J. P. et al., 2018, MNRAS, 477, 1206
Nandra K. et al., 2013, The Hot and Energetic Universe: A White Paper Presenting the Science Theme motivating the Athena+ mission, preprint, http://arxiv.org/abs/1306.2307
Nandra K., O'Neill P. M., George I. M., Reeves J. N., 2007, MNRAS, 382, 194
Nardini E. et al., 2019, A&A, 632, A109
Nelson D. et al., 2015, Astron. Comput., 13, 12
Nelson D. et al., 2018, MNRAS, 475, 624
Nelson D. et al., 2021, The IllustrisTNG Simulations: Public Data Release, preprint, http://arxiv.org/abs/1812.05609
Ni Y. et al., 2022, MNRAS, 513, 670

Ni Y., Chen N., Zhou Y., Park M., Yang Y., DiMatteo T., Bird S., Croft R., 2024, The Astrid Simulation: Evolution of black holes and galaxies to z=0.5 and different evolution pathways for galaxy quenching, preprint, http://arxiv.org/abs/2409.10666
Oogi T. et al., 2023, MNRAS, 525, 3879
Pacaud F. et al., 2006, MNRAS, 372, 578
Pakmor R. et al., 2023, MNRAS, 524, 2539
Peca A. et al., 2023, ApJ, 943, 162
Pillepich A. et al., 2018a, MNRAS, 473, 4077
Pillepich A. et al., 2018b, MNRAS, 475, 648
Planck Collaboration VI, 2020, A&A, 641, A6
Pouliasis E. et al., 2024, A&A, 685, A97
Pu X., Luo B., Brandt W. N., Timlin J. D., Liu H., Ni Q., Wu J., 2020, ApJ, 900, 141
Ricci C. et al., 2017a, ApJS, 233, 17
Ricci C. et al., 2017b, Nature, 549, 488
Ricci C. et al., 2022, ApJ, 938, 67
Ricci C. et al., 2023, ApJ, 959, 27
Roscani V., Tozza S., Castellano M., Merlin E., Ottaviani D., Falcone M., Fontana A., 2020, A&A, 643, A43
Schaye J. et al., 2023, MNRAS, 526, 4978
Schmid C., Smith R., Wilms J., 2013, hea-www.harvard.edu/heasarc/formats/simput-1.0.0.pdf
Shakura N. I., Sunyaev R. A., 1973, A&A, 24, 337
Signorini M. et al., 2023, A&A, 676, A49
Sijacki D., Vogelsberger M., Genel S., Springel V., Torrey P., Snyder G. F., Nelson D., Hernquist L., 2015, MNRAS, 452, 575
Somerville R. S., Davé R., 2015, ARA&A, 53, 51
Springel V. et al., 2018, MNRAS, 475, 676
Terrazas B. A. et al., 2020, MNRAS, 493, 1888
Torres-Albà N. et al., 2021, ApJ, 922, 252
Ueda Y., Akiyama M., Hasinger G., Miyaji T., Watson M. G., 2014, ApJ, 786, 104
Valtchanov I., Pierre M., Gastaud R., 2001, A&A, 370, 689
Vito F. et al., 2018, MNRAS, 473, 2378
Vogelsberger M., Marinacci F., Torrey P., Puchwein E., 2020, Nat. Rev. Phys., 2, 42
Volonteri M., 2010, A&AR, 18, 279
Wang F. et al., 2021, ApJ, 908, 53
Weinberger R. et al., 2017, MNRAS, 465, 3291
Weinberger R. et al., 2018, MNRAS, 479, 4056
Willingale R., Pareschi G., Christensen F., Herder J.-W. d., 2013, The Hot and Energetic Universe: The Optical Design of the Athena+ Mirror, preprint, http://arxiv.org/abs/1307.1709
Wolf J. et al., 2021, A&A, 647, A5
Wolf J. et al., 2023, A&A, 669, A127
Xu D., Zhu Y., 2024, Astron. Comput., 48, 100838
Yan W. et al., 2023, ApJ, 951, 27
Yang G. et al., 2018, MNRAS, 475, 1887
Yang G. et al., 2023, ApJ, 950, L5
Yuan F., Narayan R., 2014, ARA&A, 52, 529
Zhang C., Ramos-Ceja M. E., Pacaud F., Reiprich T. H., 2020, A&A, 642, A17

APPENDIX A: RESOLUTION CORRECTION FOR THE EDDINGTON RATIO

The resolution corrections were calculated as follows: for each of the 11 snapshots ($z = 0$ 5, $\Delta z = 0.5$), all SMBH in TNG100-1 (1.6×10^6 $M_\odot$ baryonic mass resolution) and TNG100-2 (1.1×10^7 $M_\odot$) were retrieved. Then both distributions were binned by frequency in 100 bins. For each bin, the mean value was calculated and the ratio between the TNG100-1 and tng100-2 values was plotted as a function of the values in TNG100-2. Subsequently, polynomial fits were applied to the data to capture the trends in the corrections (see Fig. A1 for an example).

For most corrections, a single polynomial fit was unable to capture accurately the shape of the correction, even when higher order polynomials were tested, so 2 fifth-order polynomials are used for most corrections. Also, due to the low number of SMBH present at higher redshift, in the TNG100 box, the correction calculated at $z = 5$ is applied to all SMBH with a larger redshift. As shown in Fig. A1, the corrections at $z = 4.5$ and 5 are very similar, therefore, this compromise is acceptable. The coefficients of the polynomial fits are presented in Table A1.

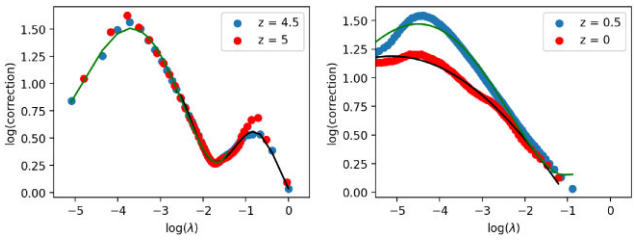

Figure A1. Left panel: the logarithm of the correction against the logarithm of the Eddington ratio, λ, for two redshifts: $z = 4.5$ (blue points) and $z = 5$ (red points). The smooth curves fit the data points at $z = 4.5$, green for log(λ) <−2 and black for log(λ) >=−2. The correction at $z = 4.5$ is very similar to the correction at $z = 5$. Right panel: the same as the left panel, but for $z = 0$ and 0.5.

Table A1. Polynomial corrections for the Eddington ratios of the TNG300-1 simulation. The polynomial is given by $\log_{10}(c) = ax^5 + bx^4 + cx^3 + dx^2 + ex + f$, where $x = \log_{10}\left(\frac{\dot{M}}{\dot{M}_{Edd}}\right)$ is the logarithm of the Eddington ratio. For most redshift intervals, two separate polynomials are used: one for high Eddington ratios ($x \geq -2$) and another for low Eddington ratios ($x < -2$).

Redshift range	a	b	c	d	e	f
$z \geq 5$	0.31780	1.90456	3.49696	1.59685	−0.81864	0.05797
$z \geq 5$	0.02818	0.48614	3.38461	11.48542	17.92994	10.52881
$4.5 \leq z < 5$	−0.08044	−0.15688	−0.18515	−0.95701	−1.34354	0.01552
$4.5 \leq z < 5$	−0.07063	−1.13526	−6.99940	−20.95482	−31.48083	−18.81004
$4.0 \leq z < 4.5$	0.05670	0.53467	1.11348	0.18469	−0.90595	0.01670
$4.0 \leq z < 4.5$	0.02399	0.48463	3.81766	14.28906	24.61804	16.15502
$3.5 \leq z < 4.0$	0.30591	2.06795	4.69183	3.98841	0.66544	0.01872
$3.5 \leq z < 4.0$	0.09243	1.86077	14.65700	56.10323	103.60800	74.62733
$3.0 \leq z < 3.5$	−0.63885	−2.69953	−3.68593	−1.82274	−0.54234	−0.00207
$3.0 \leq z < 3.5$	−0.00255	0.01824	0.61534	3.51845	6.81554	4.55758
$2.5 \leq z < 3.0$	−0.97712	−4.55106	−7.37515	−5.01543	−1.57583	0.01368
$2.5 \leq z < 3.0$	0.01384	0.29867	2.43638	9.15021	15.19302	9.38886
$2.0 \leq z < 2.5$	−0.77190	−3.64542	−5.87739	−3.81529	−1.17848	−0.01827
$2.0 \leq z < 2.5$	0.01596	0.33515	2.66812	9.82456	16.11500	9.86593
$1.5 \leq z < 2.0$	0.07274	0.76975	2.64941	3.84594	2.01147	0.34789
$1.5 \leq z < 2.0$	0.00959	0.21865	1.87183	7.33157	12.60437	8.14784
$1.0 \leq z < 1.5$	0.03566	0.33147	1.16261	1.97365	1.23036	0.24592
$1.0 \leq z < 1.5$	0.00910	0.22525	2.09226	8.92938	16.99349	12.23198
$0.5 \leq z < 1.0$	0.00033	0.01233	0.14861	0.64626	0.58232	0.08427
$z < 0.5$	0.00012	0.00480	0.06104	0.26417	0.07170	−0.03721

This paper has been typeset from a TEX/LATEX file prepared by the author.